THESIS FOR THE DEGREE OF DOCTOR OF PHILOSOPHY

Impact of Glass Formation on the Thermal Stability of Non-Fullerene Solar Cells

SANDRA HULTMARK

Department of Chemistry and Chemical Engineering

CHALMERS UNIVERSITY OF TECHNOLOGY

Göteborg, Sweden 2023

Impact of Glass Formation on the Thermal Stability of Non-Fullerene Solar Cells

SANDRA HULTMARK

ISBN: 978-91-7905-878-4

Doktorsavhandlingar vid Chalmers tekniska högskola, Ny series nr 5344

ISSN 0346-718X

Department of Chemistry and Chemical Engineering
Chalmers University of Technology
SE-412 96 Göteborg, Sweden

Telephone: +46 (0)31-772 1000

Cover:
“ Cross-polarized optical microscope image of ITIC-4F crystals’’

Chalmers Digitaltryck

Göteborg, Sweden 2023

Impact of Glass Formation on the Thermal Stability of Non-Fullerene Solar Cells

SANDRA HULTMARK

Department of Chemistry and Chemical Engineering

Chalmers University of Technology

Abstract

The world is facing immense challenges such as climate change and the depletion of non-renewable resources, making renewable sources of energy essential for a sustainable future. Organic solar cells are emerging as a promising technology; however, their stability requires significant improvement. The nanostructure of the active layer evolves over time, especially during heating, leading to a degradation in device performance. The focus of this thesis is to improve the thermal stability of the active layer.

Firstly, the thesis studies the impact of mixing on glass formation by introducing the concept of kinetic fragility to organic semiconductors. Model systems of up to eight perylene derivatives are investigated that demonstrate an unprecedented ability to form a stable molecular glass due to aggregate formation. Next, the thesis discusses the impact of isomers on glass formation, which is illustrated with an anthradithiophene-based compound. Binary mixtures of isomers were also found to form aggregates that stabilize the liquid state. In addition, the thesis describes fragility studies of doped systems and establishes that chemical doping can affect the glass formation of a semiconducting polymer. The doped polymer shows a strong tendency for glass formation which is assigned to restricted motion of oxidized polymer chains. Furthermore, the thesis analyzes mixtures of organic photovoltaic acceptors. Binary mixtures of two indacenodithienothiophene-based acceptors are found to co-crystallize, while mixtures of three to five fused-ring non-fullerene acceptors exhibited a reduced tendency to crystallize. Finally, the thesis discusses the use of acceptor mixtures for improving the thermal stability of organic photovoltaic devices. Ternary solar cell devices with two acceptors are discussed that show a stable nanostructure and improved thermal stability compared to binary devices. The thesis also explores hexanary devices that consist of five acceptor molecules, which exhibit excellent thermal stability. Therefore, the use of multicomponent acceptor mixtures is found to be a powerful tool for creating thermally stable organic solar cells.

Keywords: organic electronics, conjugated polymers, organic solar cells, bulk heterojunction blend, glass formation, kinetic fragility, thermal stability, nanostructure.

Publications

This thesis consists of an extended summary of the following appended papers:

Paper I **Hexanary blends: A strategy towards thermally stable organic photovoltaics,** Sri Harish Kumar Paleti, Sandra Hultmark, Jianhua Han, Yuanfan Wen, Han Xu, Si Chen, Emmy Järsvall, Ishita Jalan, Diego Rosas Villalva, Anirudh Sharma, Jafar. I. Khan, Ellen Moons, Ruipeng Li, Liyang Yu, Julien Gorenflot, Frédéric Laquai, Christian Müller, Derya Baran, *Nat. Commun.,* 2023, 14, 4608

Paper II **Impact of oxidation-induced ordering on the electrical and mechanical properties of a polythiophene co-processed with bistriflimidic acid,** Sandra Hultmark, Mariavittoria Craighero, Sepideh Zokaei, Donghyun Kim, Emmy Järsvall, Furqan Farooqi, Sara Marina, Renee Kroon, Jaime Martin, Igor Zozoulenko, Christian Müller, *J. Mater .Chem C*, 2022, 11, 8091-8099

Paper III **Vitrification of Octonary Perylene Mixtures with Ultralow Fragility,** Sandra Hultmark, Alex Cravcenco, Khushbu Kushwaha, Suman Mallick, Paul Erhart, Karl Börjesson, Christian Müller, *Sci. Adv*, 2021, 7, 4659

Paper IV **Suppressing Co-Crystallization of Halogenated Non-Fullerene Acceptors for Thermally Stable Ternary Solar Cells,** Sandra Hultmark, Sri Harish Kumar Paleti, Albert Harillo, Sara Marina, Ferry Anggoro Ardy Nugroho, Yanfeng Liu, Leif Ericsson, Ruipeng Li, Jaime Martín, Jonas Bergqvist, Christoph Langhammer, Fengling Zhang, Liyang Yu, Mariano Campoy-Quiles, Ellen Moons, Derya Baran, Christian Müller, *Adv. Funct. Mater*, 2020, 2005462

Contribution report

Paper I — Performed FSC and DSC studies and analysis supervised by C.M. Carried out AFM-IR together with I.J., supervised by E.M.. R.L. performed GIWAXS measurements and L.Y. analyzed the data. S.C. conducted the TDCF studies, supervised by F.L. J.K and J.G analyzed the TDCF measurements. E.J. prepared GIWAXS samples and assisted with FSC studies. S.H.K.P fabricated OSCs devices and performed thermal stability studies supervised by D.B.. S.H.K.P prepared the first draft of the manuscript with contributions from S.H, Y.W, J.H, H.X, D.R.V and A.S. assisted with thermal stability studies. C.M. conceived the study, supervised the thermal analysis, and revised the manuscript. All authors contributed to the revision of the final version of the manuscript.

Paper II — Carried out thermal analysis with FSC and DSC and wrote the manuscript together with M.C. and S.Z. supervised by C.M.. M.C. and S.Z. carried out electrical and mechanical measurements. D.K. and I.Z. carried out molecular dynamic's simulations, E.J. carried out UV-vis spectroscopy and S.M. and J.M. carried out GIWAXS measurements. R.K. synthesized the polymer.

Paper III — Designed and performed all thermal analyses and PL measurements, analyzed the data, designed the study, planned the experiments, and wrote the manuscript with help and input from C.M.. A.C and K.K synthesized the bay-substituted perylenes under supervision of K.B.. P.E. carried out the DFT calculations. All authors assisted with writing and editing of the manuscript.

Paper IV — Carried out thermal analysis and nanostructure characterization with DSC, FSC, DMA and SEM. Performed AFM-IR studies supervised by E.M. and L.E. Performed Pl measurements together with Y.L. supervised by F.Z. and J.B. F.A.A.N. and C.L. carried out nano plasmonic resonance studies and M.C.Q. and A.H. prepared PL triangle diagrams. S.H.K.P fabricated OSCs devices, performed thermal stability studies, analyzed data supervised by D.B.. R.L. performed GIWAXS measurements and L.Y. analyzed the data. All authors assisted with writing and editing of the manuscript.

The author has published the following papers which are not included in the thesis:

Origins of the Open-circuit Voltage in Ternary Organic Solar Cells and Design Rules for Minimized Voltage Losses, Yuming Wang, Jianwei Yu1, Rui Zhang1, Jun Yuan1, Sandra Hultmark, Catherine E. Johnson, Nathaniel P. Gallop, Bernhard Siegmund, Deping Qian, Huotian Zhang, Yingping Zou, Martijn Kemerink, Artem A. Bakulin, Christian Müller, Koen Vandewal, Xian-Kai Chen, Feng Gao, *Nat. Energy*, 2023, 41560-023-01309-5

Correlating acceptor structure and blend nanostructure with the photostability of nonfullerene organic solar cells, Sri Harish Kumar Paleti, Sandra Hultmark, Nicolas Ramos, Nicola Gasparini, Abdul-Hamid Emwas, Jaime Martin, Christian Müller, Derya Baran, *Sol. RRL*, 2022, 6:2200436

Tuning of the elastic modulus of a soft polythiophene through molecular doping, Sepideh Zokaei, Donghyun Kim, Emmy Järsvall, Abigail M. Fenton, Albree R. Weisen, Sandra Hultmark, Phong H. Nguyen, Amanda M. Matheson, Anja Lund, Renee Kroon, Michael L. Chabinyc, Enrique D. Gomez, Igor Zozoulenko and Christian Müller, *Mater. Horiz.* 2021, 9, 433-443

Room temperature dye glasses: A guideline toward the fabrication of amorphous dye films with monomeric absorption and emission, Clara Schäfer, Sandra Hultmark, Yizhou Yang, Christian Müller, Karl Börjesson, *Chem. Mater*., 2022, 34, 9294-9302

Influence of synthetic pathway, molecular weight and side chains on properties of indacenodithiophene-benzothiadiazole copolymers made by direct arylation polycondensation, Desiree Adamczak, Andrea Perinot, Hartmut Komber, Anna Illy, Sandra Hultmark, Bianca Passarella, Wen Liang Tan, Sebastian Hutsch, David Becker-Koch, Charlotte Rapley, Alberto D.Scaccabarozzi, Martin Heeney, Yana Vaynzof, Frank Ortmann, Christopher R. McNeill, Christian Müller, Mario Caironi, Michael Sommer, *J. Mater. Chem. C,* 2021, 9, 4597-4606

Sequential doping of ladder-type conjugated polymers for thermally stable n-type organic conductors, Suhao Wang, Tero-Petri Ruoko, Gang Wang, Sergi Riera-Galindo, Sandra Hultmark, Yuttapoom Puttisong, Fabrizio Moro, Hongping Yan, Weimin Chen, Magnus Berggren, Christian Müller, Simone Fabiano, *ACS Applied Materials & Interfaces*, 2020, 12, 53003-53011

Diffusion-Limited Crystallization: A Rationale for the Thermal Stability of Non-Fullerene Solar Cells, Liyang Yu, Deping Qian, Sara Marina, Ferry A. A. Nugroho, Anirudh Sharma, Sandra Hultmark, Anna I. Hofmann, Renee Kroon, Johannes Benduhn, Detlef-M. Smilgies, Koen Vandewal, Mats R. Andersson, Christoph Langhammer, Jaime Martín, Feng Gao, and Christian Müller, *ASC Appl. Mater. Interfaces*, 2019, 11, 21766-21774

A Record Chromophore Density in High-Entropy Liquids of Two Low-Melting Perylenes: A New Strategy for Liquid Chromophores, Khushbu Kushwaha, Liyang Yu, Kati Stranius, Sandeep Kumar Singh, Sandra Hultmark, Muhammad Naeem Iqbal, Lars Eriksson, Eric Johnston, Paul Erhart, Christian Müller, Karl Börjesson, *Adv. Sci, 2019, 6, 1801650.*

Roll-to-roll Dyed Conducting Silk Yarns: A Versatile Material for E-Textile Devices, Anja Lund, Sozan Darabi, Sandra Hultmark, Jason D. Ryan, Barbro Andersson, Anna Ström, Christian Müller, *Adv. Mater. Technol, 2018, 3, 1800251*

Table of Contents

1 Introduction

The importance of global energy demand cannot be understated as it is necessary to sustain modern society. The world consumes around 28000 TWh (2022) of energy and this value is expected to increase by 50% by 2050.[1-2] Today, more than 75% of the energy that we use comes from fossil fuels.[3] Fossil fuels meet the world's current energy needs, but contribute to issues like global warming, polluted air, and acid rain due to the produced gases of CO_2, SO_2 and NO_2.[4] In 2015, a historic agreement was concluded in Paris, the Paris agreement, where countries agreed to work together to fight the climate crisis. The agreement aims e.g., to limit the increase in global average temperature to below 2 ℃ and preferably keep it at 1.5 ℃. To achieve this, global emissions must be halved by 2030 and reach close to zero by 2050.[5] Therefore, it is necessary to stop using fossil fuels and find alternative renewable energy sources.

The current global energy and climate crisis as well as the shortfalls in fossil fuels from certain parts of the world further enhance the need for renewable sources of energy.[6] Currently, renewable energy only covers 22% of the global energy supply and the goal is an increase to 40% by 2030.[7] Therefore, it is necessary that a bigger proportion of the energy is supplied via clean renewable resources. Solar energy is an excellent alternative because the sun provides one year of the world's energy consumption, in just one hour.[8] It is also clean, free, and reliable. To harness the energy from the sun one can, use solar panels that utilize solar energy to heat water or solar cells that provide electricity by harvesting sunlight.

In 1839, Alexander Becquerel demonstrated that electricity can be generated directly from solar energy via the photovoltaic effect, which involves the conversion of photons into an electrical current.[9] However, it was not until 1954 that Daryl Chapin, Calvin Fuller and Gerald Pearson developed the first functional solar cell made from monocrystalline silicon with an efficiency of 6%.[10] Since then, solar cells technologies have continued to evolve and expanded into four generations of solar cells:

- *First-generation* solar cells, also called conventional or traditional solar cells, primarily consist of crystalline silicon and currently dominate the market due to their high efficiency of up to around 27% and their lifespan of approximately 25 years. While these solar cells possess advantages such as stability and efficiency, they suffer from inflexibility, high production cost, and significant weight.[11-13]
- *Second-generation* solar cells are based on thin layers of amorphous silicon, copper indium gallium selenide or cadmium telluride with an efficiency of up to 23%. Compared to first-generation solar cells the advantage of this type is that these are more cost-effective as they require less material, have lower weight, and have some degree of flexibility. However, they still consume significant energy during production since they are, like first generation solar cells, made with vacuum processes, which require a significant amount of energy.[11, 13]
- *Third-generation* solar cells offer cost-effective high efficiency solutions. This category includes various types of solar cells such as organic, perovskite, copper zinc tin sulfide, quantum dots, and dye sensitized solar cells.[14]
- *Fourth-generation* solar cells, also called multijunction cells, have an efficiency of up to 45%. These are hybrid solar cells that combine the flexibility of third generation solar cells with the stability of first- and second-generation solar cells.[15-16]

Organic solar cells (OSCs) are composed of organic materials such as small organic molecules or polymers. OSCs are now approaching 20 % in lab-scale efficiency, which does not reach the efficiencies of several other third generation solar cells, yet they have other advantages which makes the development of these solar cells important.[17-20] Unlike traditional solar cells, OSCs can be processed directly from solution by printing or coating techniques facilitating scalability and thus reducing costs. In addition, they are made from materials that are readily available, and the devices are both flexible and lightweight. Furthermore, an increase in the growth of the Internet of Things (IoT), the exchange of data between devices, will require energy for the sensors that measure e.g., moisture, temperature, or other parameters. Instead of replacing expensive batteries, it may be possible to integrate OSCs with these sensors. One example can be found in the work of the Swedish company Epishine, which is optimizing OSCs to harness energy from indoor lighting for use with indoor IoT sensors.[21]

One drawback with OSCs is the stability that must be improved to achieve longer lifetime and higher durability. Typically, OSC printing is performed at temperatures up to 140 ℃ to ensure fast evaporation of solvents.[22-23] Printing of the hole transport layer also requires similar temperatures; however, this high temperature causes the nanostructure of the BHJ to undergo phase separation or crystallization.[24-25] Even if the efficiency and stability of the OSC are not yet comparable to other generation solar cells, there is a lot of potential and large-scale production has already been achieved. To improve the stability of OSCs it is important to understand and control the evolution of the nanostructure of the active layer. In this thesis, the use of multicomponent mixtures is explored to improve the thermal stability of BHJs. The first chapter provides an overview of basic device design, whereas chapter 3 and 4 discuss glass formation, kinetic fragility, and nanostructure stability. Finally, chapter 5 focuses on OSC thermal stability.

2 Organic solar cells

This chapter describes some general concepts of organic solar cells, OSCs.

2.1 Conjugated polymers and organic semiconductors

In OSCs, the photoactive layer that absorbs the sunlight is mainly comprised of donor and acceptor materials. The donor material absorbs sunlight to excite electrons that are donated to the acceptor material. The donor material is usually a polymer, but it can also be a small molecule and it needs a broad absorption range in the solar spectrum. They consist of a carbon backbone with alternating double and single bonds. The most commonly known polymer donor is poly(3-hexylthiophene-2,5-diyl) (P3HT) but due to the high bandgap and low absorption range, other alternative donor polymers were investigated.[26-27] Researchers began using low-bandgap polymer donors. Low-bandgap polymers consist of an electron-rich part and an electron-poor part that broadens the absorption.[28-32] For example, the low-bandgap polymer donors PTB7-Th and PM6 used in this thesis exhibit a much broader absorption than P3HT (see molecular structures in Figure 2.1).

The acceptor material accepts the electrons from the donor material, and it is usually a small molecule. Acceptor molecules are classified into fullerene and non-fullerene acceptors (NFAs). Previously, fullerene and its derivatives such as $PC_{71}BM$ and $PC_{61}BM$ were the dominant acceptors but because of their low absorption, poor thermal and photochemical stabilities, NFAs were explored instead. NFAs are made up of A-D-A type backbones with derivatives from perylene and pentacene, for instance, ITIC-4Cl, ITIC-4F and Y6 and its derivatives used in this thesis (Figure 2.1).[33-39]

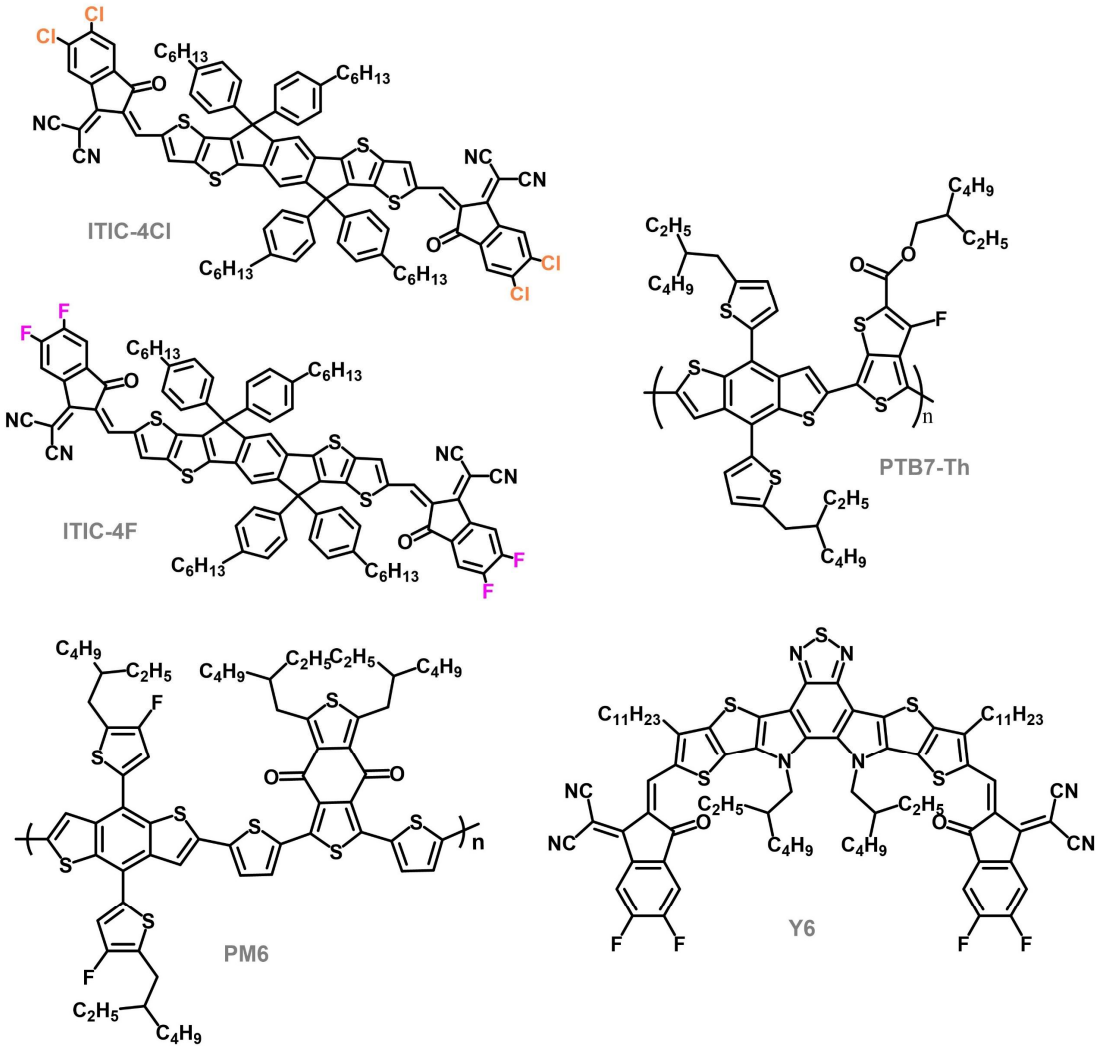

Figure 2.1. Chemical structure of the donor polymers PTB7-Th and PM6 and the acceptor molecules ITIC-4F, ITIC-4Cl, and Y6.

Organic small molecules and polymers are carbon-based materials. Carbon has four valence electrons. Take ethene as an example: its carbons have three electrons in sp^2 orbitals that form single bonds (σ-bonds) and the remaining electron of each carbon resides in a p-orbital, forming a double bond (π-bond) (Figure 2.2). Conjugated systems with alternating single and double bonds enable electron delocalization along the π-bonds. The two bonding orbitals σ and π are lower in energy and antibonding σ^* and π^* orbitals are formed at higher energy levels. For ethene, the π-orbital is the highest occupied molecular orbital (HOMO) and the antibonding π^*-orbital is the lowest unoccupied molecular orbital (LUMO).[40]

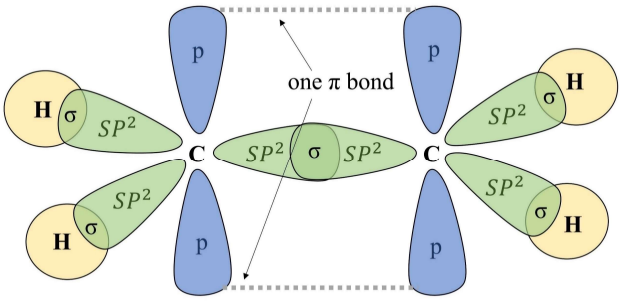

Figure 2.2. Orbital picture of ethene.

Conductors can be classified according to their bandgap size i.e. the difference in HOMO (conduction band) and LUMO (valence band), which decides the minimum energy needed to excite an electron.[32] Metals do not have a bandgap while insulators have a large bandgap. Larger conjugation lowers the bandgap and improves semiconducting properties. Semi-conductors in the neutral state behave as isolators but upon doping they become conductive.[41] Alan J. Heeger, Alan Mac Diarmid and Hiedeki Shirakawa won the Nobel Prize in 2000 for the discovery of conducting polymers.[42]

2.2 Device architecture

There are two main types of organic solar cell architectures: the conventional and inverted device architecture.[43] The main difference is the direction of charge flow, where conventional cells absorb light through the anode side and inverted cells through the cathode side. The inverted architecture is used in this thesis (Figure 2.3). In this structure, the transparent material indium tin oxide (ITO) is deposited on a transparent substrate (PET or glass) and used as the cathode and on top of this a thin layer of ZnO nanoparticles is spin-coated that function as the electron transport layer.[44-45] The next layer is the active layer, which is the light absorbing layer that separates photons into electrons and holes. Next is a molybdenum oxide (MoO) layer as a hole transport layer. Poly(3,4-ethylenedioxythiophene) polystyrene sulfonate (PEDOT:PSS) is also a commonly used hole transport layer material.[46-48] The hole transport layer facilitates hole extraction from the active layer. Finally, a silver electrode is evaporated and functions as the anode.

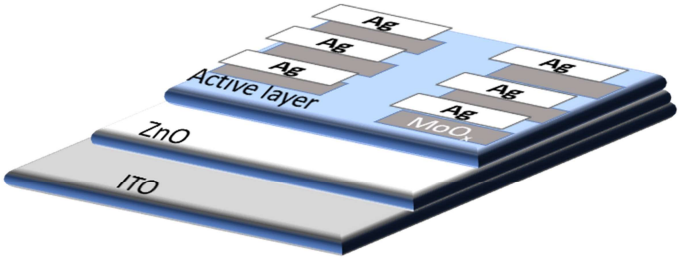

Figure 2.3. Device architecture with ITO as the cathode, ZnO as the electron transport layer, the active layer, MoO_x as the hole transport layer and silver as the anode. Adapted with permission from ref [49]. Copyright 2020 Wiley.

2.3 Working principles

Organic solar cells, like all solar cells, convert sunlight into electricity by converting photons into electrons and holes. A photon, with an energy bigger than the semiconductor bandgap, enters the device through the transparent anode or cathode (cf. 2.2 Device architecture) and into the semiconductive photoactive material. Absorption of the photon excites an electron from HOMO to LUMO and an electron-hole pair is formed, an exciton. The exciton diffuses until it recombines or until it reaches a donor-acceptor interface, where a charge transfer complex (CT) is formed at the interface.[50] The exciton must separate into electrons and holes for the solar cell to generate electricity.[51] If the exciton is generated in the donor phase, another semiconductive material with lower LUMO is used, causing the excited electron to be transfer to the lower LUMO level. If the exciton is generated in the acceptor phase, the hole is donated to the molecule with high HOMO. Electrons then diffuse to the anode and the holes to the cathode by hopping from one energetic site to another, generating current (Figure 2.4).[52] To ensure efficient electron diffusion, Fermi levels of the cathode and anode should match the LUMO and HOMO of the acceptor and donor, respectively. Electron and hole transport layers are incorporated to modify these work functions but also to reduce the contact resistance and to promote or block one type of charge carrier.[53]

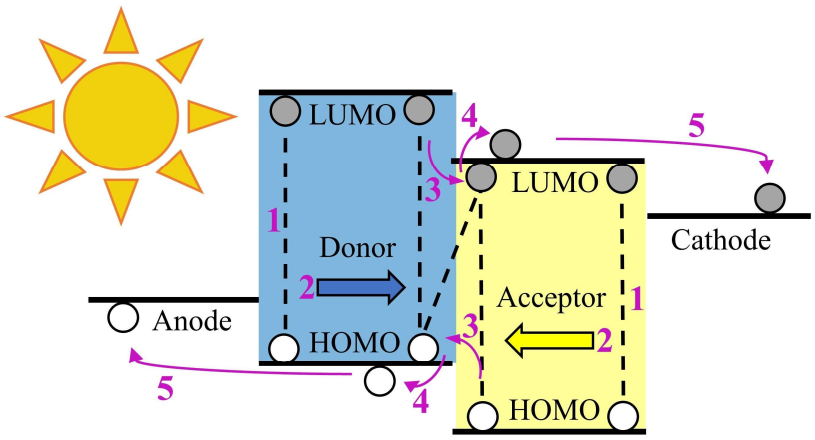

Figure 2.4. Working principle of an organic solar cell. (1) Donor and acceptor material absorbs light, and an exciton is formed. (2) The exciton diffuses towards the donor-acceptor interface. (3) a charge transfer complex (CT) is formed at the interface. (4) The exciton separates into free charges. (5) The charges diffuse to their respective electrodes and current is generated.

In OSCs, recombination is the main mechanism of loss wherein two charge carriers of opposite charges combine. There are two different recombination processes: geminate and non-geminate recombination. Geminate recombination occurs when the electron and hole that originate from the same photon recombine immediately after dissociation at the donor-acceptor interface. Non-geminate recombination, on the other hand, arises from different dissociated charges merging via e.g., trap states. Recombination via trap states occurs in two steps. In the first step, a free charge carrier gets trapped and is unable to diffuse, then in the second step an opposite charge carrier combines with the trapped charge carrier.[54-56]

2.4 Bulk-heterojunctions

To maximize photon absorption, the thickness of the active layer should not be too thin since thicker layers absorb more light. However, if it is too thick, the charge transport pathway becomes too long, which may increase charge recombination. Furthermore, an exciton has a limited lifetime and can only diffuse 1-10 nm before it recombines.[57] Therefore, the acceptor-donor interface should be within 1-10 nm from the point where the exciton is

generated. As a result, it is very important to optimize the active layer thickness to achieve an optimal performance. Solar cells made by bilayers are not a good alternative because parts of the absorbing material are more than 1-10 nm away from the donor-acceptor interface, which results in charge recombination.

The best way to increase the donor-acceptor interfacial area in the OSC active layer is through bulk heterojunction, BHJ, blends. In a BHJ blend, the acceptor and donor material are mixed in a common solvent and distributed during solidification as mixed and/ or pure phases throughout the photoactive layer.[58-59] The exciton can travel further in a crystalline phase than in an amorphous phase and crystalline phases also improve the charge mobility.[60] To generate electricity, the electrons must be collected at the anode and holes at the cathode. In a bilayer solar cell, the donor material and the acceptor material are separated, which makes it easy for the electrons and the holes to travel to the respective electrode. In a BHJ blend, in the ideal case, an interconnected network is formed with pathways to maintain percolation in the mixture in order to ensure a continuous transport of electrons.

2.5 I-V characteristics

To evaluate the performance of a solar cell, a lamp using standard AM 1.5G illumination with an intensity of 1 sun (1000 Wm^{-2}) is used. Solar cells are exposed to light and at the same time the photocurrent output is measured. The photocurrent output is then normalized to the solar device area and plotted against applied voltage, resulting in J-V curves. These curves can be used to extract four distinct parameters (Figure 2.5):

The open circuit voltage (V_{oc}) is the voltage achieved when the photocurrent is zero. The maximum value is determined by the difference in HOMO of the donor material and LUMO of the acceptor material plus a loss factor of 0.6 eV and is related to the energy of the charge transfer state.[61-62]

The short circuit current (J_{sc}) is the photocurrent with zero voltage applied and is given by the number of absorbed photons. J_{sc} provides information about charge separation and charge transport in the solar cell and is affected by various factors including the nanostructure, the thickness of the active layer, the extinction coefficient, charge carrier mobility and lifetime.

The fill factor (FF) is given by the ratio between the maximum electric power (P_{max}) and power from the product of J_{sc} and V_{sc}:[52]

$$FF = \frac{P_{max}}{J_{sc} \cdot V_{sc}} \qquad \text{(eq. 2.1)}$$

The power conversion efficiency (PCE) is the overall efficiency of the solar cell, and it corresponds to the ratio between the maximum generated electric power and the power of the incident light (P_{in}):[52]

$$PCE = \frac{P_{max}}{P_{in}} = \frac{FF \cdot J_{sc} \cdot V_{oc}}{P_{in}} \qquad \text{(eq. 2.2)}$$

A typical J-V curve is shown in Figure 2.5**.** Another way to evaluate solar cell performance is to measure Internal Quantum Efficiency (IQE) or External Quantum Efficiency (EQE). IQE is the ratio between the number of charge carriers and the number of absorbed photons at a given wavenumber. EQE is the ratio between the number of charge carriers collected by the solar cell and the incident photons at a given wavenumber.

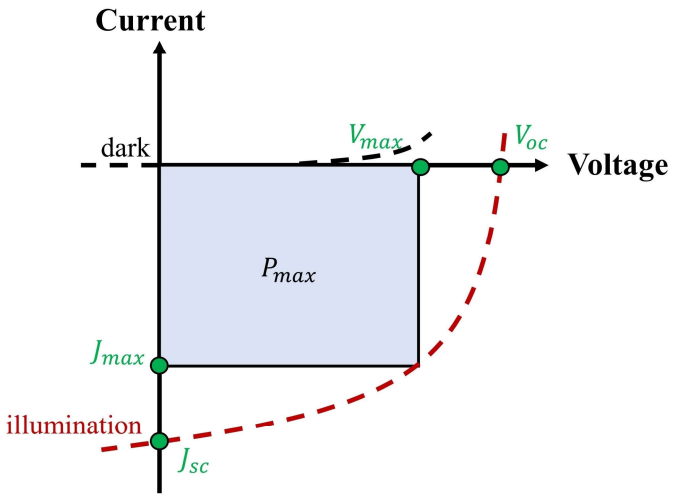

Figure 2.5. Schematic of a JV-curve showing the photovoltaic characteristics under illumination (red dashed curve) and in dark (black dashed curve).

2.6 Coating techniques and sample preparation

Spin-coating is a coating technique utilized in the lab to dispense the BHJ active layer evenly on a surface.[63-64] The substrate is mounted on a sample holder using vacuum. A droplet of the solution containing the active materials is dropped onto the surface and the sample spins with a high speed to distribute the liquid uniformly while the solution evaporates (Figure 2.6). This technique provides the advantage of achieving a coating layer of the desired thickness by altering the viscosity of the solution or coating speed. Due to the small size, the spin coater can be placed in a glovebox or in a fume hood. However, a major disadvantage is that it cannot be applied to large-scale manufacturing processes that require continuous production.

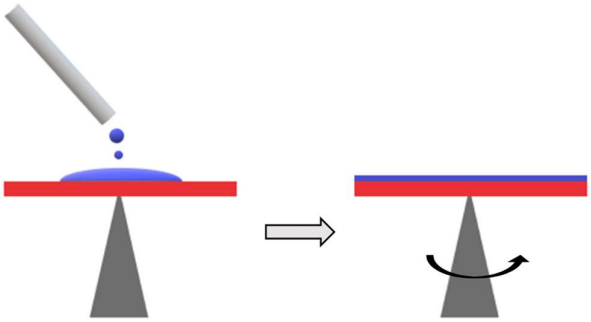

Figure 2.6. Spin-coating. The liquid solution is dropped on the substrate and the sample spins with a certain speed to distribute the liquid.

Since organic solar cells are processed from solution, they can easily be upscaled with printing techniques such as blade coating or slot die coating. However, the coating speed is dependent on the rate of solvent removal, which can be accelerated by heating. The choice of substrate determines the highest possible processing temperature, e.g. 140 ℃ in the case of Polyethylene terephthalate, PET, foil.[22-23] Nonetheless, OSCs possess poor thermal stability and at high temperature the nanostructure may undergo coarsening or crystallization. Addressing this issue is crucial to achieve longer lifetime and higher durability of OSCs.

3 Glass formation and nanostructure stability

Glass formation and the role of disordered solids are of fundamental importance not only in the context of OPVs, but in many scientific disciplines. Efficient control over the stability of these devices is essential for this evolving technology. The solidification of the OSCs active layer takes place upon evaporation of the solvent, which is preferably fast to ensure high-throughput manufacturing.[22-23] However, the solidified nanostructure is not in thermodynamic equilibrium because the material is not given enough time to crystallize or adopt a relaxed confirmation and thus form a stable disordered solid.[65] This results in the evolution of the nanostructure over time, especially at elevated temperature. Typically, phase separation and crystallization are detrimental to device performance, long-term stability, and reproducibility.[66-68] Consequently, glass formation is important in maintaining thermal stability by preventing the reorganization of the nanostructure. This chapter provides an overview of phase separation and crystallization as well as kinetic and thermodynamic aspects for glass formation. Finally, various techniques to detect the glass transition temperature, T_g, are presented.

3.1 Phase separation and crystallization in BHJ blends

Evolution of the nanostructure occurs through phase separation or crystallization of any of the blend components. The process of phase separation results in purification creating domains that are rich in one of the components. When BHJ blends are processed, phase separation occurs as the solvent evaporates. Depending on the composition and rate of solvent removal the blend undergoes binodal or spinodal decomposition.[69]

Fast solidification, quenches the mixture into the spinodal regime where phase separation occurs due to density driven fluctuations without an energy barrier, resulting in diffuse domain boundaries.[69-70] The nanostructure of a blend that undergoes spinodal decomposition will continue to coarsen, unless frozen in below the T_g of the blend. Binodal decomposition, instead, occurs when a homogeneous donor/acceptor mixture during slow solidification has sufficient time for a nucleation and growth type process, resulting in two phases with sharp boundaries (Figure 3.1). Nucleation is associated with an energy barrier and work is needed to form a nucleus of a critical size. Here, two contrasting elements come into play, the difference in

volume free energy of the homogeneous and phase-separated state, ΔG_{ls}, and the interfacial energy associated with the nucleus surface, γ. The work associated with the formation of a spherical nucleus with radius *r* is given by:[71]

$$W(r) = -\frac{4\pi}{3} r^3 \Delta G_{ls} + 4\pi r^2 \gamma \qquad \text{(eq. 3.1)}$$

The maximum work required to create a nucleus of critical size *r** is represented by the energy barrier *W**. By solving $\mathrm{d}W(r)/\,\mathrm{d}\,r = 0$, the critical radius can be determined:

$$r^* = \frac{2\gamma}{\Delta G_{ls}} \qquad \text{(eq. 3.2)}$$

Therefore, the energy barrier is given by:[72-73]

$$W(r^*) = \frac{16\pi\gamma^3}{3\Delta G_{ls}^2} \qquad \text{(eq. 3.3)}$$

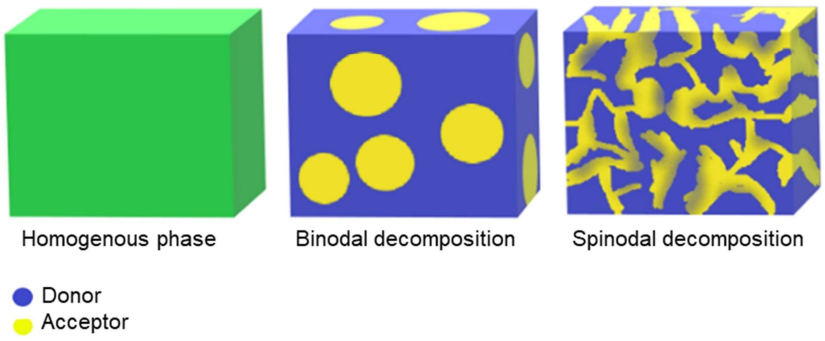

Figure 3.1. Nanostructure arising due to spinodal and binodal decomposition.

To achieve an optimal device performance, a blend system requires arrangement of donor and acceptor molecules with a specific degree of order. However, prolonged crystallization of the blend components could result in larger crystals that reduce the interface where CT can occur. Crystallization can arise from a homogeneous blend of the components or from an already phase-separated domain that is enriched with the component undergoing crystallization. The latter process operates akin to a two-step crystallization mechanism in case phase separation precedes crystallization.[74] The process of crystallization, similar to binodal decomposition, involves a nucleation and growth step:[75-76]

$$nucleation \text{ rate} \propto D(T) \cdot \exp\left(-\frac{W^*}{kT}\right) \qquad \text{(eq. 3.4)}$$

$$growth \text{ rate} \propto D'(T) \cdot \left[1 - \exp\left(-\frac{\Delta G_{ls}}{kT}\right)\right] \qquad \text{(eq. 3.5)}$$

Where ΔG_{ls} is the difference in volume free energy of the liquid and crystalline state ($\Delta G_{ls} = G_l - G_s$) and the energy barrier for nucleation is $W^* \propto \Delta G_{ls}^{-2}$ which decreases with undercooling.[77] Favorable conditions for crystallization (product of nucleation and growth rate) occur at temperatures between T_g and T_m, where both diffusion and ΔG_{ls} are finite. The rate of nucleation and growth are influenced by both kinetic and thermodynamic factors. They both require the diffusion of molecules to the nucleation site and growth front, respectively, and therefore scale with the diffusion coefficient ($D \propto \eta^{-1}$) of the system.[78] In addition, there is a thermodynamic driving force for crystallization, which is determined by the difference in free energy between the disordered liquid and crystalline state. This opens the possibility to hinder and control crystallization by both thermodynamic and kinetic means, which are discussed further in section 3.3.

Factors such as the interaction between donor, acceptor and processing solvent, and with the substrate as well as molecular weight and processing temperature all contribute to the degree of phase separation during solvent removal.[69] A good solvent means that there are strong interactions between the donor/acceptor and the solvent, e.g., through hydrogen bonds. A bad solvent means that the donor and acceptor prefer interaction with itself and remain separate from the solvent.

3.2 Interplay of T_g and nanostructure stability

The BHJ nanostructure that is obtained once the solvent has evaporated is usually not in thermal equilibrium and can change over time, especially when exposed to heat, which can be utilized as a tool to further improve the nanostructure but may also cause gradual device degradation. Gradual coarsening of the BHJ nanostructure can occur through phase separation or crystallization of either blend component. For many blend systems a certain amount of order (crystallinity) and crystal size is required to optimize the device performance. However,

continued crystallization of the blend components can result in larger crystals, which may negatively impact charge generation. The T_g is a useful parameter to distinguish between regimes where phase separation and crystallization occur slowly, or rapidly.

3.2.1 Evolution of the nanostructure below T_g

The T_g is commonly defined as the temperature at which the conformational relaxation time of molecules is around 100 seconds.[79] When the temperature is far below the T_g only movement of short segments or side/pendant groups in the amorphous part of the polymer or local relaxation in case of small molecules can occur. An example of this is observed in blends of TQ1 and $PC_{61}BM$, which have a T_g of 110 ℃, but still undergo local changes up to 70 ℃ below the T_g, leading to a slight improvement in photocurrent when annealing devices below T_g.[80] In contrast, PCBM crystallization is typically not observed below T_g since diffusion of the acceptors is too slow. Therefore, the T_g has often been identified as a critical parameter for thermal stability in the fullerene related OPV literature.

Ghasemi et al. reported the diffusion coefficients of various NFAs in different polymer matrices across a wide range of temperatures, extending below the T_g of the acceptor or BHJ blend.[81-82] The diffusion coefficient of NFAs at 80 ℃ ranges from 10^{-23} to 10^{-12} cm^2s^{-1}, depending on the combination of NFA and donor polymer, resulting in slow mass transport in NFA based BHJs below T_g.[82] Some NFA/polymer blends, such as di-PDI:PDBD-T, exhibit a sufficiently low extrapolated diffusion coefficient of around 10^{-20} cm^2s^{-1} at 80 ℃, indicating high thermal stability under device stability testing. Nevertheless, some BHJs based on NFAs may undergo crystallization of the acceptor at temperatures below T_g. For instance, ITIC and PBDB-T blends have a high T_g of 180 ℃ but are susceptible to acceptor crystallization at temperatures as low as 100 ℃.[83] The high propensity for ITIC molecules to crystallize likely arises through π−π interactions by the planar structure (Figure 3.2). The resultant nanometer-sized crystals are not necessarily detrimental to the BHJ nanostructure, they represent a metastable state as further changes would require melting of NFA nanocrystals followed by recrystallization.

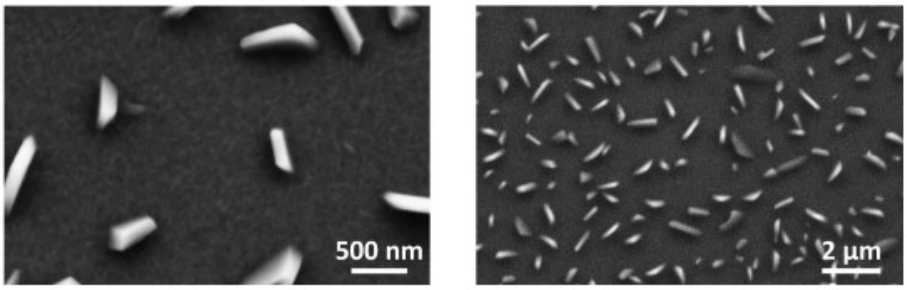

Figure 3.2. ITIC crystallization at 160 ℃ which is below the blend T_g of 180 ℃. Adapted with permission from ref [83]. Copyright 2019 ACS Publications.

3.2.2 Evolution of the nanostructure above T_g

When the temperature rises above T_g, long segments start to move in the amorphous part of the polymer and small molecules diffuse in the polymer matrix, which enables long-range mass transport that can lead to fast phase separation and crystallization. This process is often observed with fullerenes, resulting in the formation of micrometer-sized crystals that harm device performance.[67] NFAs experience a more intricate crystallization behavior as many acceptors can develop multiple polymorphs.[84] Regardless, NFAs can also reach a high degree of crystallinity. For example, ITIC-4F forms micrometer-sized crystalline domains in PTB7-Th after annealing above the blend T_g at 220 ℃ that are visible as spherulites in films examined with polarized optical microscope (Figure 3.3). The process of crystallization starts from a nucleation point. In case of polymers, it initiates when the polymers aligned themselves in plates called crystalline lamella. Without a thermal gradient, crystal growth proceed in all directions as additional lamellas are incorporated resulting in spherulites where the ordered lamellae plates are interrupted by amorphous regions.[85] For small molecules, instead, nucleation occurs when a small nucleus form (clusters of molecules) that then grow into crystals.[86]

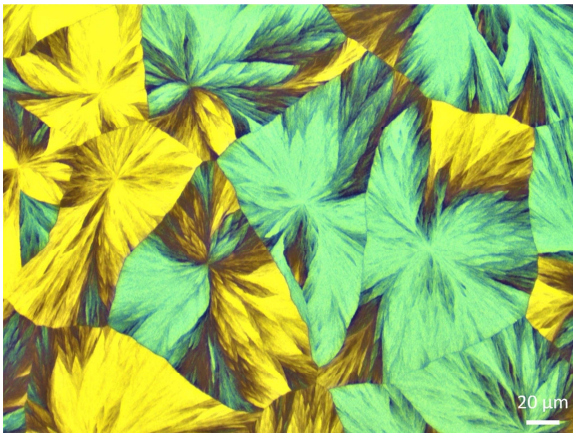

Figure 3.3. Cross-polarized optical microscope image of ITIC-4F crystals in a thin film of PTB7-Th:ITIC-4F after annealing above the blend T_g at 220 ℃ for 10 min.

3.3 Vitrification of phases

Vitrification refers to the arresting of the evolution of phases in a material through cooling below T_g. Glass formation effects both phase separation and crystallization and is influenced by both kinetic and thermodynamic factors.

3.3.1 Kinetic strategies for glass formation

Kinetic strategies to arrest phase separation and/or crystallization aim at reducing the diffusion of donor and acceptor molecules. This can be done in many ways, e.g., by using a donor or an acceptor with a high T_g. The effective T_g of mixed domains lies between the T_g of the donor and acceptor.[87] Separate domains, feature a T_g closer to the neat donor or acceptor and consequently, a BHJ blend film can show several T_g transitions, one for each type of domain.[88-89] The diffusion of fullerene and NFA acceptor derivatives can drastically decrease when mixed with a donor with a high T_g.[66, 81, 90] There are some general design rules that allow to create donors and acceptors with a high T_g. Limiting the flexibility of the main chain or small molecule through the incorporation of stiff units or bulky pendant groups. Also, decreasing the free volume through a high M_w or short alkyl side chains as well as

crosslinking increase the T_g.[91-92] Additionally, intramolecular forces such as hydrogen bonds or polar interactions increase the T_g. For example, Schaefer et al. increased the T_g of a BODIPY based molecule by balancing the attractive π–π interactions of the BODIPY core by attaching alkyl chains as steric hindrance creating BODIPY glasses at room temperature.[93] Crosslinking can be achieved by covalently linking donor and/or acceptor molecules aided by specific additives that act as molecular locks or stimuli from e.g. temperature or light that triggers a crosslinking reaction.[94-96] For example, fullerene acceptors can be linked by illuminating the fullerene blends.[97-100] In case of NFAs this dimerization approach has been mimicked by covalently connecting several acceptor molecules already during synthesis, e.g. di-PDI, which is unable to crystallize and therefore remains disordered even when annealed above the blend T_g.[101-102]

3.3.2 Thermodynamic strategies for glass formation

Mixtures of several different components have been explored as a strategy to reduce the phase separation and crystallization and thereby increase the glass-forming ability. Mixing of several compounds changes the Gibbs free energy according to:

$$\Delta G_{mix} = \Delta H_{mix} - T\Delta S_{mix} \quad \text{(eq. 3.6)}$$

Mixing is thermodynamically favorable when $\Delta G_{mix} < 0$. In case of components with no net interaction (ideal solution), the change in enthalpy of the mixture will be zero, $\Delta H_{mix} = 0$. In that case, the change in free energy upon mixing solely depends on the change in entropy upon mixing:[77]

$$\Delta S_{mix} = -Nk_B \sum_i \emptyset_i ln\emptyset_i \quad \text{(eq. 3.7)}$$

Where N represents the number of molecules, k_B is the Boltzmann constant and $\emptyset_i$ is the molar fraction of component i. The highest ΔS_{mix} is obtained with equal mol fractions of each component in the mixture (Figure 3.4). However, in the case of a polymer, the term $\emptyset_i ln\emptyset_i$ is divided by the degree of polymerization, which significantly reduces the term ΔS_{mix}. Figure 3.4 shows how the ΔS_{mix} changes for different ratios of PTB7-Th:ITIC-4F:ITIC-4Cl. If a polymer donor with a higher M_w was used, then the ΔS_{mix} would solely depend on the composition of the acceptors. Therefore, the miscibility of polymers is primarily determined by ΔH_{mix} which is calculated, in case of a nonideal solution, according to:

$$\Delta H_{mix} = TNk_B \sum_i^j \chi_{ij} \emptyset_i \emptyset_j \quad \text{(eq. 3.8)}$$

Where T is the temperature, i and j represent the different molecules and $\chi(T)$ is the Flory Huggins interaction parameter. Information regarding the equilibrium composition and the amorphous-amorphous interaction parameter χ_{aa} can be obtained from scanning transmission X-ray microscopy (STXM) or secondary ion mass spectroscopy (SIMS) measurements, while DSC can be utilized to estimate the crystalline-amorphous interactions χ_{ca}.[103-106]

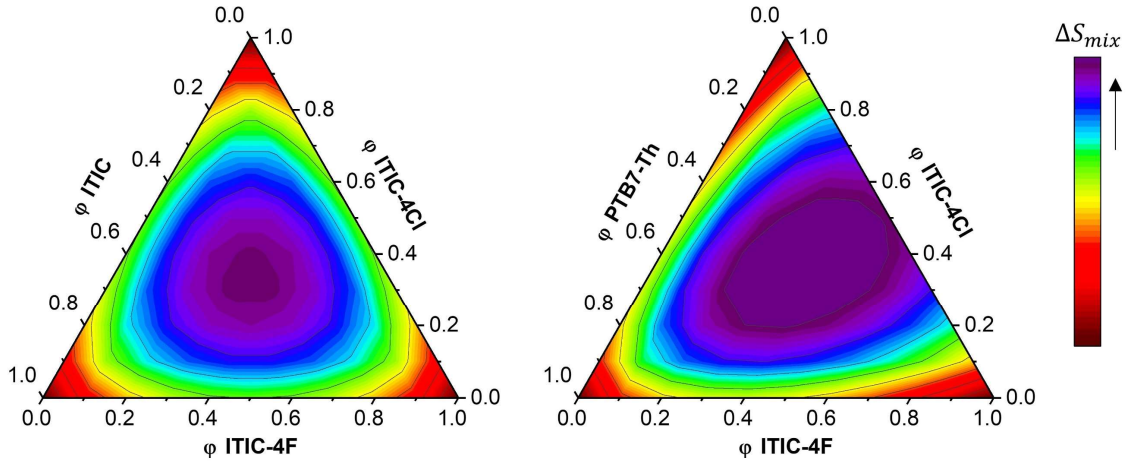

Figure 3.4. Illustration of the change in ΔS_{mix} with different mol fractions φ of three small acceptor molecules with similar molecular weights ITIC:ITIC-4Cl:ITIC-4F and the blend of a donor polymer and the two acceptors PTB7-Th:ITIC-4Cl:ITIC-4F.

For an ideal solution, for which $\Delta H_{mix} = 0$, the Gibbs free energy is decreased by $\Delta G_{mix} = -T\Delta S_{mix}$ where ΔS_{mix} increases with the number of components in the mixture. As a result, the melting temperature decreases from T_m to T_m' upon mixing and the driving force for crystallization at temperature T decreases from ΔG_{ls} to $\Delta G_{ls}'$ (Figure 3.5). The depression of the driving force reduces both the rate of crystal nucleation and growth below T_m', meaning that the blend components will crystallize more slowly (equation 3.4 and 3.5).[77]

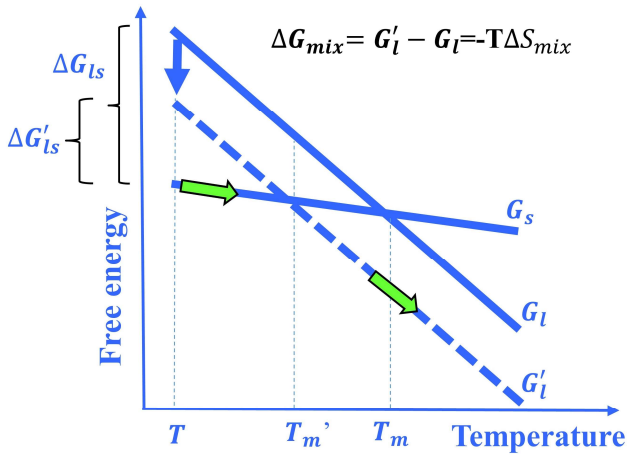

Figure 3.5. For an ideal solution, the Gibbs free energy decreases upon mixing and the green arrows show the thermodynamically favorable phase. As a result, the melting temperature decreases from T_m to T_m' and the driving force for crystallization at temperature T decreases from ΔG_{ls} to ΔG_{ls}' upon mixing.

3.4 Predicting and measuring of thermal transitions

Melting of polymer crystals occurs over a wide temperature range. This is because they contain different sizes with different lamellar thickness L_c. The Gibbs-Thomson equation can be used to estimate the T_m:[107]

$$T_m = T_m^0 \left(1 - \frac{2\sigma}{L_c \delta_c \Delta H_c^0}\right) \quad \text{(eq. 3.9)}$$

Where δ_c is the density of the crystal and σ is the surface free energy. The Fox equation is a useful tool for predicting the T_g of amorphous mixtures and random copolymers:[108]

$$1/T_{g,mix} = \sum_i \omega_i / T_{g,i} \quad \text{(eq. 3.10)}$$

Where $T_{g,mix}$ is the glass transition temperature of the mixture, $T_{g,i}$ is the glass transition temperature of each component and ω_i is the mass fraction of each component. However, for the equation to be applicable, the components in the mixture need to have similar solubility parameters. If T_m of a material is known, then the T_g can be crudely estimated according to

$T_g \sim \frac{2}{3} T_m$. Several different techniques can be utilized to measure the T_g such as variable temperature ellipsometry, dilatometry, broadband dielectric spectroscopy (BDS), nano plasmonic resonance, dynamic mechanical analysis (DMA), differential scanning calorimetry (DSC) and fast scanning calorimetry (FSC). The last three methods will be explained in detail below.

3.4.1 Dynamic mechanical analysis (DMA)

DMA involves evaluating a material's elastic and viscous response when subjected to a small periodic stress and strain. This is achieved by applying a sinusoidally changing force with known amplitude to the material while monitoring the deformation as a function of frequency, time, or temperature. For viscoelastic materials, an applied oscillating stress $\sigma(t)$ gives rise to a strain, $\varepsilon(t)$. The resulting $\varepsilon(t)$ is shifted by a phase angle of δ:[109]

$$\varepsilon(t) = \varepsilon_0 \sin(\omega t + \delta) \qquad \text{(eq. 3.11)}$$

where ε_0 is the amplitude of the strain, t is the time and ω is the angular frequency. Figure 3.6 shows the oscillating $\sigma(t)$ and $\varepsilon(t)$ response.

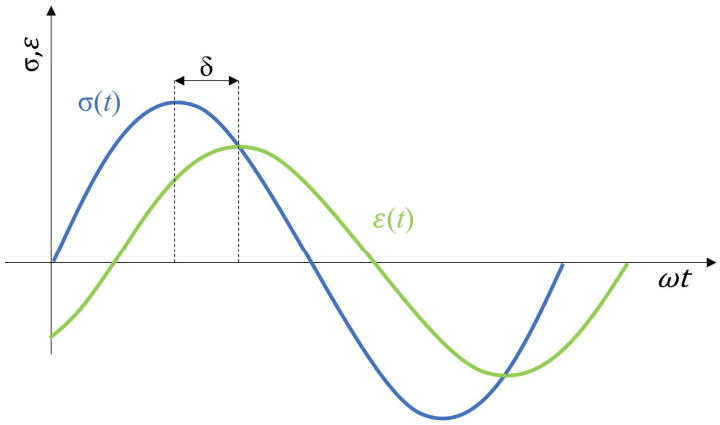

Figure 3.6. The applied oscillatory stress $\sigma(t)$ (blue) and the strain response $\varepsilon(t)$ (green).

σ(t) is composed of the storage modulus, E', that is in phase with the strain and the loss modulus E'' that is out of phase with the strain:

$$E' = \frac{\sigma_0}{\varepsilon_0} \cos \delta \quad \text{(eq. 3.12)}$$

$$E'' = \frac{\sigma_0}{\varepsilon_0} \sin \delta \quad \text{(eq. 3.13)}$$

E' is the real component and E'' is the imaginary component of the complex modulus (E^*). E' is the modulus of elastic deformation and corresponds to the materials ability to store energy per unit volume, indicating the materials stiffness.[109-110] The E'' is the modulus of plastic deformation and represents the amount of dissipated energy per unit volume and is directly related to the heat released during this process. Furthermore, the loss factor tan δ, which is the energy dissipation factor of a material, can be determined by dividing the loss modulus by the storage modulus:

$$\tan \delta = \frac{E''}{E'} \quad \text{(eq. 3.14)}$$

A sample preparation technique utilized to study conjugated polymers by Shima et al. was employed in this thesis to detect the T_g with DMA.[88] In this method, a glass fiber mesh is coated with a solution of the material to be examined (Figure 3.7). The glass fiber mesh is cut at a 45° angle to avoid continuous glass fibers along the length of the sample. The substrate is then positioned in the DMA instrument and subjected to a certain heating rate and frequency, ω, to determine the T_g. This method cannot measure the absolute values of E'' and E' since the effective cross-sectional area of the investigated material cannot be defined. One key advantage of this approach is that the T_g is measured directly for thin films rather than bulk samples, requiring only a small amount of around 4 mg of material.

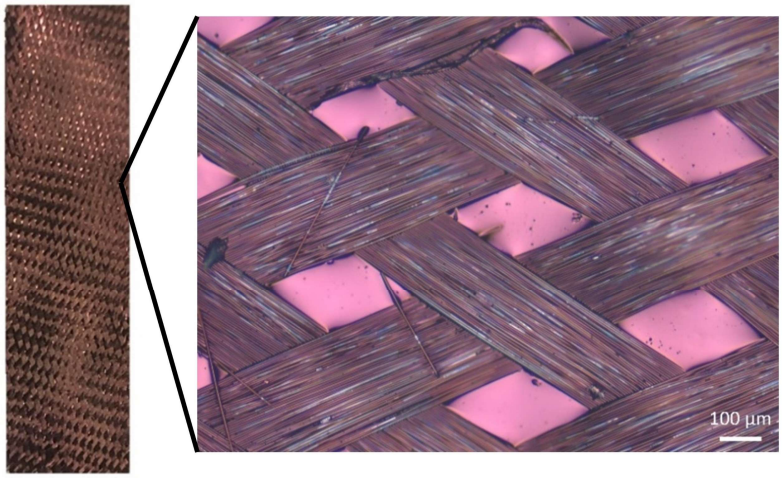

Figure 3.7. Optical microscope image of a glass fiber mesh coated with PTB7-Th:ITIC-4F:ITIC-4Cl.

Figure 3.8 illustrates the mechanical properties of the ternary blend PTB7-Th:ITIC-4F:ITIC-4Cl as a function of temperature measured at a frequency of 1 Hz. The region below T_g, with the highest E' is the glassy state. Around the T_g, E' decreases significantly with increasing temperature. E' increases above the T_g possibly because of crystallization. The T_g corresponds to the peak in tan δ which would shift to a higher temperature with a higher frequency. For PTB7-Th:ITIC-4F:ITIC-4Cl a T_g = 200 ℃ is obtained (Figure 3.8).

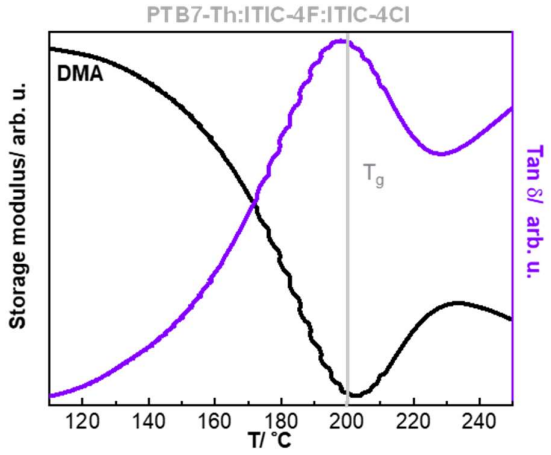

Figure 3.8. DMA measurement of PTB7-Th:ITIC-4F:ITIC-4Cl reinforced with a glass fiber mesh. Adapted with permission from ref [49]. Copyright 2020 Wiley.

3.4.2 Differential scanning calorimetry (DSC)

In this thesis, a heat flux DSC was employed which is a technique used to gather information about thermal transitions of a material. In the DSC, a pan that contains the sample and an empty reference pan are placed in a furnace on a sample holder connected by a thermoelectric disk. As the furnace is heating at a constant rate, heat is transferred to the sample and the reference pan. The difference in temperature of the sample and reference pan, ΔT, which is related to the heat capacity, C_P, of the sample, is recorded. The change in heat flow is calculated by Ohm's law:[111]

$$\frac{\mathrm{d}H}{\mathrm{d}t} = \frac{\Delta T}{R} \qquad \text{(eq. 3.15)}$$

Where H is enthalpy in J mol^{-1} and R is the thermal resistance of the thermoelectric disk. The change in heat flow is then plotted against the temperature to create a DSC thermogram that reveals the phase transitions of the sample. The heat flow signal is related to C_P according to:

$$\frac{\mathrm{d}H}{\mathrm{d}t} = C_P \frac{\mathrm{d}T}{\mathrm{d}t} + f(T,t) \qquad \text{(eq. 3.16)}$$

Where C_P is the samples specific heat capacity in J K^{-1}mol^{-1} and $f(T,t)$ is kinetic response of the sample in J mol^{-1}.[111-112] T_g can be seen as an endothermic step-wise change as there is an increase in C_P of the sample while heating through T_g (Figure 3.9). Below T_g in the glassy state, the material is hard and brittle and only short segmental motions or vibrations of atoms are

possible. Between T_g and T_m, long segments (polymers) or small molecules in the amorphous part of the material can move and the material is soft and/or rubbery in the case of a completely amorphous material or hard in case of a semi-crystalline material. Above T_m in the liquid state, crystals have molten, and entire chains or small molecules move freely. The area under the melting or crystallization peak corresponds to the enthalpy of melting, ΔH.

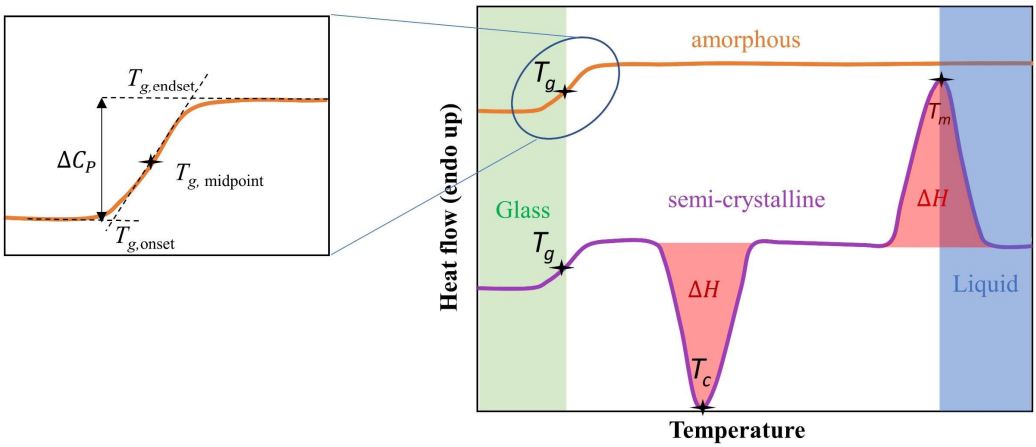

Figure 3.9. Example of a DSC thermogram for amorphous and semi-crystalline material were $T_{g,\text{midpoint}}$, $T_{g,onset}$, $T_{g,endset}$ and ΔC_p are marked.

3.4.3 Fast scanning calorimetry (FSC)

FSC is a method similar to DSC but it allows much faster heating and cooling rates of up to 40 000 K s^{-1} and -1000 K s^{-1}, respectively, which can be used to avoid crystallization.[113] One advantage with FSC is that only a very small amount of sample (in ng) is needed. FSC cannot easily measure absolute values of heat flow since the weight of the material is unknown. Material is placed next to a reference sample on a small chip sensor (Figure 3.10). There are several different ways to place the sample on the sensor e.g. through casting a small droplet directly on the sensor, by placing the material on the sensor or by spin coating the material on the sensor. In the latter case, the reference is covered with glycose while the sample is spin coated on top of the sensor and the glycose is then removed with water. It is possible to remove the glucose without having water in contact with the sample, but if the sample is very water sensitive it is better to use another of the above-mentioned sample preparation methods.

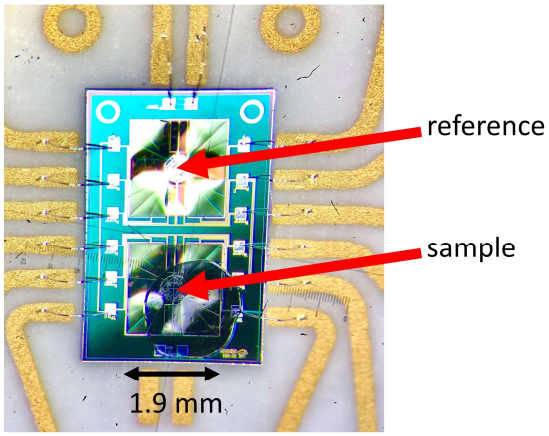

Figure 3.10. Chip sensor from Mettler Toledo with reference and sample.

3.5 Physical aging experiments with FSC

With FSC, physical aging experiments can be performed to detect the T_g. The sample is first heated to above T_m to delete the thermal history, and then annealed at different temperatures for 30 min. Another heating cycle after quenching the material directly from above T_m to below T_g is also performed as a reference scan (Figure 3.11.a). Reorganization of molecules to an

equilibrated thermodynamic state takes place below the T_g if given enough aging time, which depends on the annealing temperature.[114] This reorganization results in an endothermic overshoot in an FSC heating scan. The enthalpy overshoot first grows and then decreases in magnitude as the T_g is approached (the orange marked peaks in Figure 3.11.b). At the same time the overshoot shifts to higher temperatures. This is because with a higher annealing temperatures molecules adopt a relaxed confirmation and form a stable disordered solid, therefore the molecules need a higher temperature to reach the liquid state upon heating. When equilibrium is reached at the lower limit of the T_g, the enthalpy overshoot disappears. Instead, a melting peak appears because crystals are now formed during aging. In case of the ternary PTB7-Th:ITIC-4F:ITIC-4Cl, the enthalpy change ΔH goes to zero at T_{anneal} = 205 °C, which is the upper limit of the T_g (Figure 3.11.b).[115]

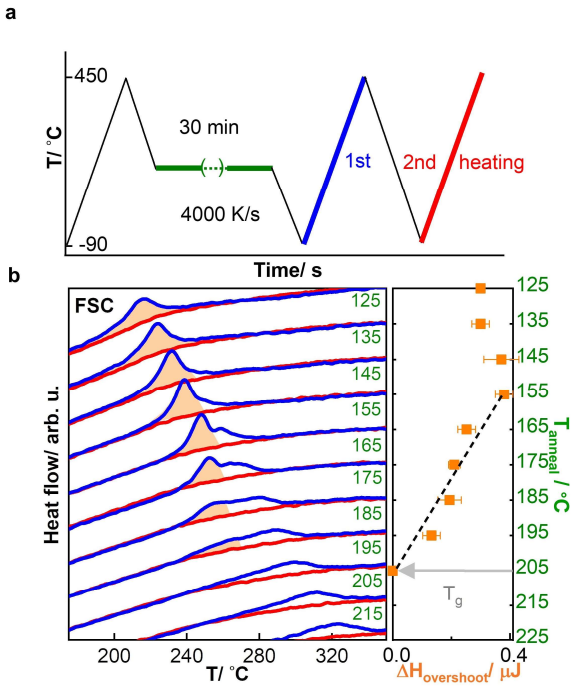

Figure 3.11. a) FSC protocol with heating after annealing (blue) and a reference heating after quenching (red) b) FSC heating scans of 1:0.5:0.5 PTB7-Th:ITIC-4F:ITIC-4Cl after annealing (blue) and after quenching (red) with the enthalpy overshoot indicated in orange. Adapted with permission from ref [49]. Copyright 2020 Wiley.

3.6 Glass transition temperature of acceptors and donors

Many NFAs have a higher T_g compared to fullerene acceptors. For instance, ITIC, Y6 and many of their derivatives have a T_g > 180 ℃, which is higher than PCBMs and other NFAs (see Table 3.1 for a comparison). Since the T_g of many donor polymers is lower, for example 125 ℃ for PTB7-Th (Figure 3.12), the effective T_g of finely mixed BHJ blends lies between the T_g of the donor and acceptor.[49, 87]

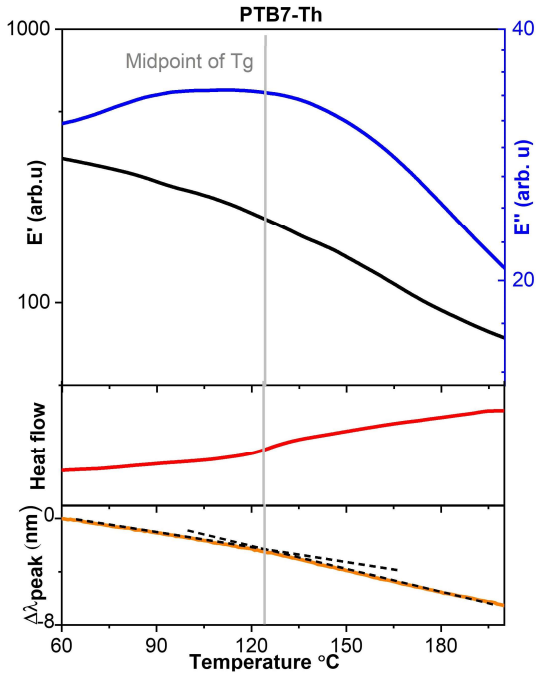

Figure 3.12. Different methods to measure the T_g of PTB7-Th. DMA heating thermogram showing the storage modulus E' (black) and loss modulus E'' (blue), DSC heating thermogram (red) and plasmonic nano spectroscopy measurement (orange). Adapted with permission from ref [49]. Copyright 2020 Wiley.

Table 3.1. Glass transition temperature, T_g, of different donor and acceptor materials measured with variable temperature ellipsometry, DMA, FSC or DSC.

Donor / acceptor	Measurement technique	T_g (°C)	Ref
PCE10 (PTB7-Th)	DMA, DSC, plasmonic nanospectroscopy	125	Unpublished
PCE13	DMA	80	Unpublished
PBDBT-2Cl	DMA	87	Unpublished
PIDTBT	DMA	71	Unpublished
$PC_{61}BM$	ellipsometry / DSC	110 / 131, 139	[115-117]
$PC_{71}BM$	DSC	163	[118]
ITIC	FSC	180	[83]
ITIC-4F	FSC	185	[49]
ITIC-4Cl	FSC	210	[49]
ITIC-M	DSC	180	Unpublished
Y6	FSC	206/ 205	Unpublished/ [119]
di-PDI	FSC	160	Unpublished

4 Kinetic fragility

The kinetic fragility index, *m*, is a measure of how rapidly the dynamics of a liquid slowdown in the vicinity of the T_g and it can be used to classify glass formers as strong or fragile.[120] This chapter describes the concept of *m*, how to measure it with FSC and its importance for the field of organic electronics, specifically OPVs.

4.1 How to measure kinetic fragility?

The kinetic fragility of a liquid refers to its ability to reorganize into a more energetically favorable arrangement as the temperature decreases and approaches T_g. It is determined by the steepness of the normalized temperature dependence of a logarithmic dynamic property *x*, at T_g, where *x* can be viscosity or relaxation time:[120-122]

$$m = \left.\frac{\mathrm{d}\log x}{\mathrm{d}(T_g/T)}\right|_{T=T_g} \qquad \text{(eq. 4.1)}$$

According to Austen Angell liquids categorized as strong glass formers display minimal changes around the T_g and exhibit nearly Arrhenius dynamics over a broad temperature range.[120] These materials with $m < 40$, tend to form a molecular glass because the viscosity, η, tends to be relatively large compared with the viscosity of a fragile material at a given $T > T_g$ (Figure 4.1). The viscosity of a fragile glass former can instead be described with the Vogel-Fulcher-Tammann (VFT) equation:[123-125]

$$\eta(T) = \eta_0 \exp\left(\frac{B}{T-T_0}\right) \qquad \text{(eq. 4.2)}$$

Where η_0 is the value of the viscosity at infinite temperature, T_0 is the temperature at which the viscosity becomes infinite, and *B* is a constant. Materials with a high *m* have a lower viscosity at a given $T > T_g$ compared with strong glass formers, which increases the likelihood of crystallization (Figure 4.1).

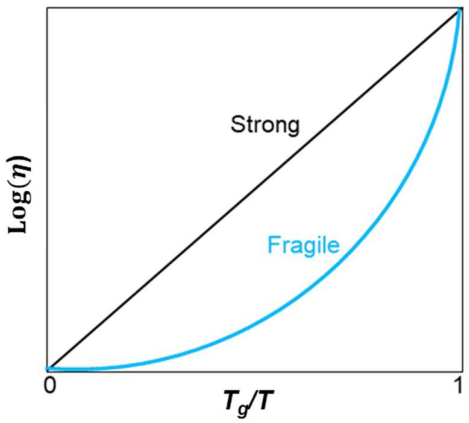

Figure 4.1. Angell plot with log(η) vs T_g/T showing the trend for strong (black line) vs fragile (blue line) glass formers.

Traditional methods for creating glasses lead to an amorphous solid by cooling a material from a liquid state to below the T_g. The properties of the resulting glass are influenced by the cooling rate. Over time, glasses relax and release excess energy because of non-equilibrium of glassy materials and the propensity of moving towards equilibrium.[65] This process is known as aging, and results in low-energy molecular packing that may involve an increase in density, modules, and kinetic stability.[126] Various methods, including DMA, rheology, and FSC, may be utilized for determining m. For rheology, a minimum of 40 mg of the sample must be provided for each measurement, unless a small plate can be used. DMA, on the other hand, is solely appropriate for polymers as it necessitates the material to be in the form of a free-standing film. Consequently, FSC was adopted in this thesis for fragility measurements, as presented in Table 4.1.

To determine m with FSC, the cooling rates, q, are plotted versus the change in limiting fictive temperature, T_f', deduced from heating scans after cooling at different rates. T_f' is the temperature at which the liquid freezes into a glass. It has been shown that log(q) against $1/T_f'$ has the same slope as log(η) against $1/T$ with the assumption that the structural relaxation rate is a function of the viscosity of the melt.[127] T_f' increases with increasing cooling rate and strong glass formers have a wider range of T_f's compared to fragile glass formers (Figure 4.2.a). In case of FSC, the material is first heated to a temperature above T_m (much above T_g in case of amorphous material) then cooled to below T_g with cooling rates ranging from -0.1

to -1000 K s^{-1}, followed by a fast heating scan (Figure 4.2.b). Moynihan's area matching method is used to calculate T_f' if it is above $T_{g,onset}$, (Figure 4.2.c):[128-130]

$$\int_{T_f'}^{T\gg T_g}(C_{pl}-C_{pg})dT = \int_{T\ll T_g}^{T\gg T_g}(C_p-C_{pg})dT \quad \text{(eq. 4.3)}$$

where C_{pl} is the heat capacity of the liquid, C_{pg} is the heat capacity of the glass and C_p is the apparent heat capacity of the sample. If the T_f' is below the $T_{g,onset}$, a simplified extrapolation method is used, (Figure 4.2.c):[122, 131]

$$\int_{T_f'}^{T\gg T_g}(C_{pl}-C_{pg})dT = 0 \quad \text{(eq. 4.4)}$$

After determining T_f' from the different heating scans an Angell plot is constructed by plotting $-\log|q|$ vs. $T'_{f,ref}/T_f'$ where $T'_{f,ref}$ is obtained from DSC heating thermograms at 0.17 K s^{-1}. The fragility can then be extracted from the slope close to T_g:[122, 128-129]

$$m = \left.\frac{-\mathrm{d}\log|q|}{\mathrm{d}(T'_{f,ref}/T_f')}\right|_{T=T'_{f,ref}} \quad \text{(eq. 4.5)}$$

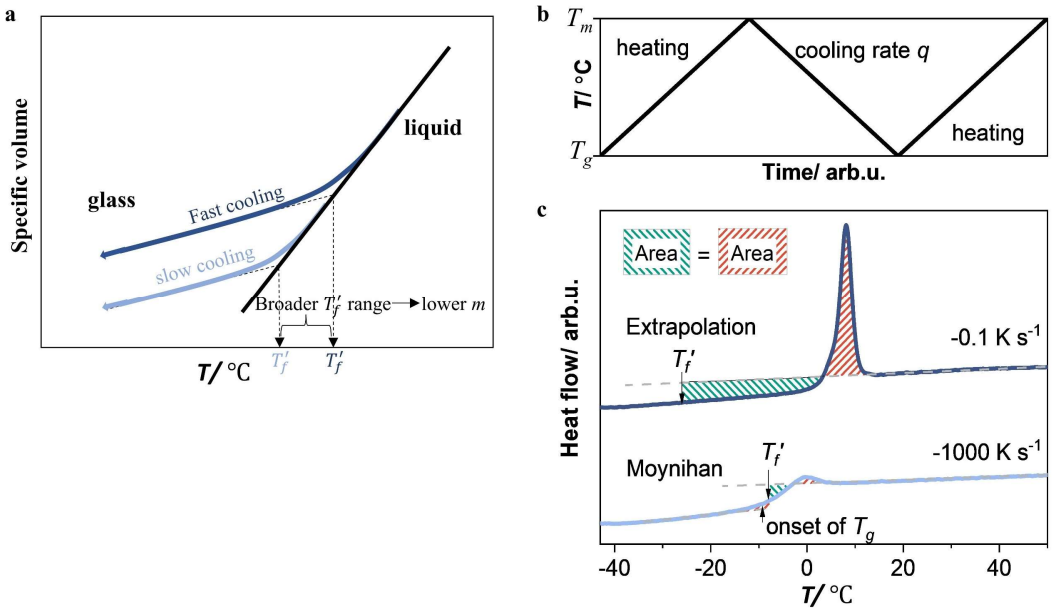

Figure 4.2. a) Plot of specific volume vs. temperature showing T_f' during fast (dark blue) vs. slow (light blue) cooling. b) FSC protocol: The sample is first heated to a high temperature and then cooled with different cooling rates followed by fast heating. c) Heating scans after slow (dark blue) vs fast (light blue) cooling and their respective T_f'. Adapted with permission from ref [132]. Copyright 2021 Science Advances.

Table 4.1. Different techniques to measure the T_g and m. In this thesis FSC was used to measure m.

Technique	**Glass transition temperature, T_g**	**Fragility, m**
Differential scanning calorimetry	yes	no
Fast scanning calorimetry	yes	yes, was used in this thesis
Dynamic mechanical analysis	yes	yes
Broadband dielectric spectroscopy	yes	no
Shear rheometry	yes	yes
Nanoplasmonic resonance spectroscopy	yes	no
Variable temperature ellipsometry	yes	no

4.2 Kinetic fragility and the relevance for OSCs

Glass formation is often linked to fragility, making it of significant practical interest for the thermal stability of OSCs. In most cases, good glass formers possess a higher viscosity η between T_g and T_m compared with fragile glass formers, which suppresses nucleation and growth of crystals (eq. 3.4 and 3.5). Mass transport of acceptor molecules through the polymer matrix is influenced by η, which is inversely proportional to the diffusion coefficient, D, according to the Stokes-Einstein relation, i.e. $D \propto \eta^{-1}$. Therefore, a lower viscosity results in a higher diffusion coefficient. For example, the VFT equation (eq. 4.2) can be used to describe the temperature dependence of the diffusion coefficient of PCBMs when blended with various donor polymers.[133] Hence, PCBM-based blends likely are fragile materials, consistent with crystallization above T_g. The diffusion coefficient of PCBM at 80 ℃ is $D \approx 10^{-10}$-10^{-9} cm^2s^{-1}, on the other hand, NFAs such as IT-M and IEICO-4F exhibit a lower diffusion coefficient of $D \approx 10^{-15}$-10^{-14} cm^2s^{-1} (P3HT as donor)[82, 105, 134], indicating less rapid long-range mass transport in case of NFA based BHJs. The reason for the lower diffusion of NFs could be due to the planar structure of ITIC derivatives, which may require collective motion of adjacent molecules for relaxation to take place. Kinetic fragility measurements therefore may serve as an indicator for the OSC stability and may provide understanding related to phase separation and crystallization in BHJ blends.

4.3 Kinetic fragility of semiconductor mixtures

Even though the fragility of various organic molecules has been reported, including o-terphenyl and m-xylene with m values of 76 and 56, respectively, minimal emphasis has been placed on assessing the impact of mixing on the fragility.[135] A comprehensive understanding of the evolution of the active layer nanostructure is imperative for enhancing the stability of OSCs. This section explores the utilization of multi-component semiconductor mixtures to enhance the glass-forming ability and, consequently, heighten the thermal stability of OSCs, which is covered in chapter 5.

4.3.1 Perylene mixtures

In this project mixing of perylene molecules with different pendant groups was studied (see molecular structures in Figure 4.3).

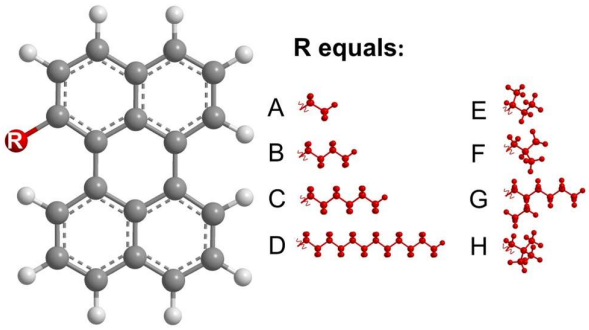

Figure 4.3. Molecular structures of bay-substituted perylene derivatives. Adapted with permission from ref [132]. Copyright 2021 Science Advances.

To gain an understanding of how the perylene blends affect the glass forming ability, the impact of mixing on the reduced glass transition temperature, defined as $T_{rg}=T_g/T_m$, was examined. The T_{rg} varies between 0.4 and 0.85 for any glass forming material. The glass-forming tendency is improved with increasing T_{rg}.[136] Instead, a decrease in T_{rg} is associated with a fast nucleation rate. Perylene derivatives A, B and C, each with an individual T_{rg} of about 0.7, were mixed and analyzed. DSC heating scans from solution-cast material revealed that T_m decreases upon mixing while T_g was unaffected. Consequently, mixtures with higher concentrations of any of the three molecules had a measurable but increased T_{rg} of up to 0.78 (Figure 4.4). On the other hand, binary and ternary mixtures with the components present in close to stoichiometric ratios did not experience crystallization (no measurable T_m) indicating a greater tendency for glass formation.

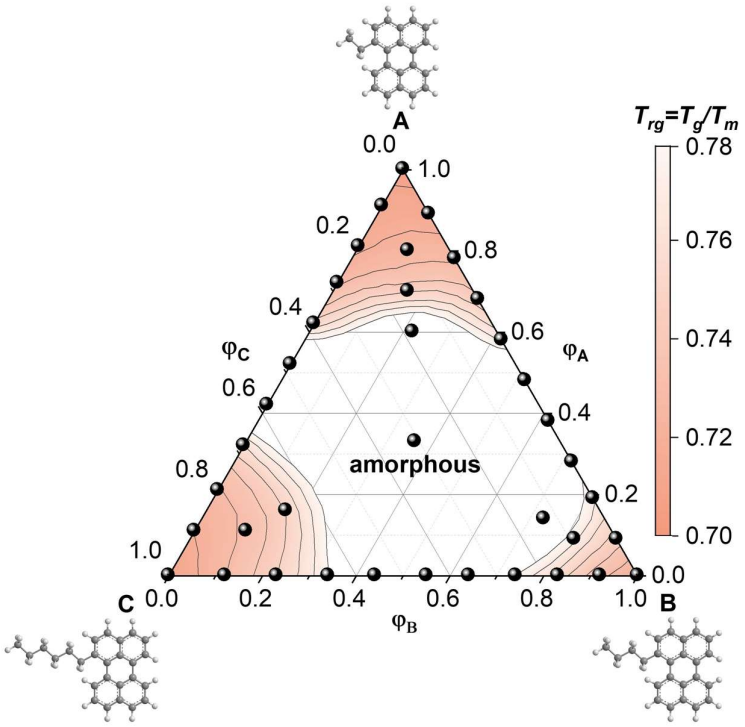

Figure 4.4. Reduced glass transition temperature T_{rg} of A:B:C mixtures with different stoichiometries determined using the T_g and T_m values extracted from DSC first-heating scans. Adapted with permission from ref [132]. Copyright 2021 Science Advances.

The effect of mixing on the fragility was then determined by examining perylene mixtures that comprised an equal weight of each component. All perylenes A-H feature a high *m* ranging from 71 to 97. The fragility decreased with the number of components in the mixture and a value of *m*=13 ± 2 was determined for the octonary mixture, which is lower than values reported for the strongest known organic and inorganic glass formers such as *o*-xylene with *m* = 55, *m*-fluorotulene with *m* = 45, SiO_2 with *m* = 20 or low-density amorphous water with *m* = 14 (Figure 4.5a).[137-138] The Angell plot of the octonary mixture revealed two regimes with different slopes for fast and slow cooling suggesting a liquid-liquid transition when cooled at low rates (Figure 4.5b).

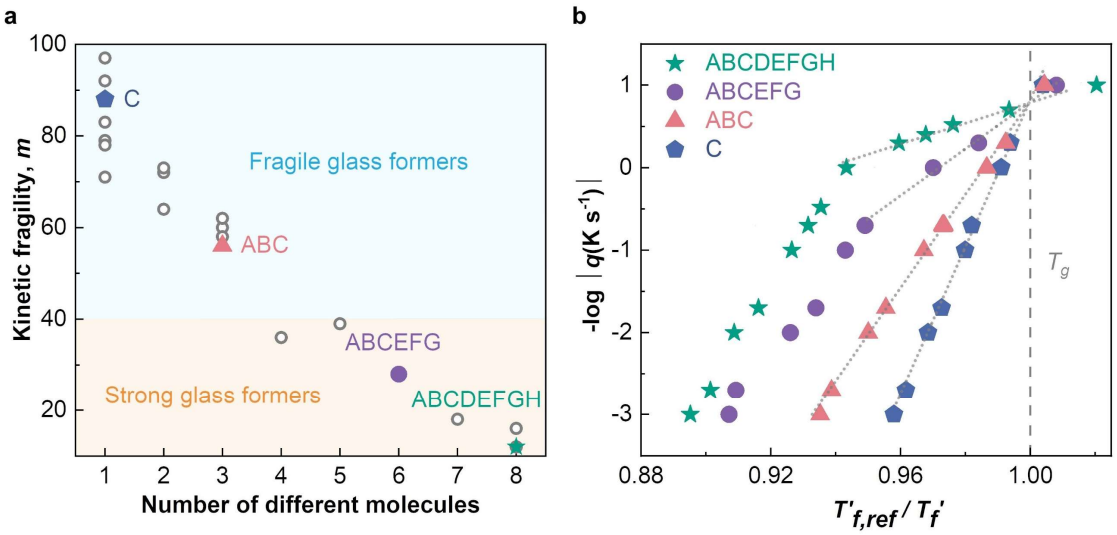

Figure 4.5. a) Kinetic fragility plotted as a function of the number of perylene derivatives in the mixture. b) Fragility plot. Adapted with permission from ref [132]. Copyright 2021 Science Advances.

To confirm that a liquid-liquid transition takes place, photoluminescence spectroscopy (PL) was employed. The PL spectra of the drop-cast octonary mixture revealed a peak at 590 nm, typical for aggregates. At a temperature of 150 °C, the emission shifts to 470 nm typical for monomers (Figure 4.6.a). Fast cooling maintains the monomeric state while slow cooling results in a redshift to 590 nm indicating that the perylene mixture formed aggregates (Figure 4.6.b). We hypothesize that mixed stacks of perylenes form aggregates with a high ΔS_{mix} (eq 3.7), allowing for the stabilization of the liquid since collective motion of a significant number of molecules is required for structural relaxation, which reduced the fragility to the ultralow value of $m = 13 \pm 2$ observed for the octonary mixture. The stabilized glass has a high energy barrier for crystallization since molecules need to separate before they can crystallize.

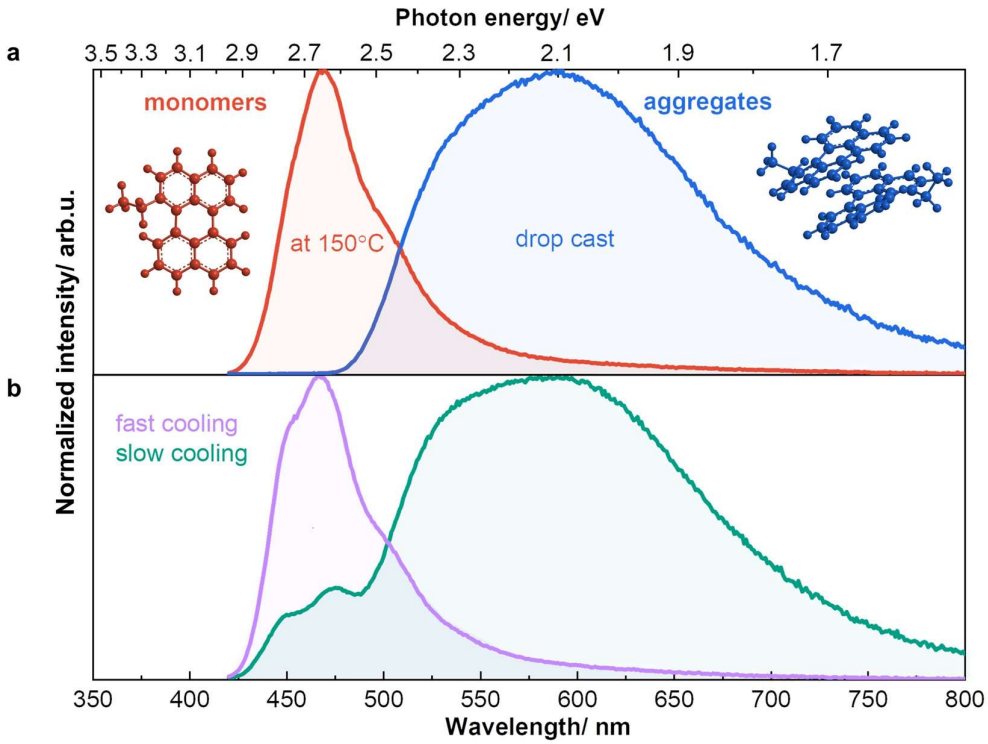

Figure 4.6. Emission spectra of the octonary mixture for a) drop-cast material, at 150 ℃ and b) after fast and slow cooling of the material from 150 ℃ to -40 ℃. Adapted with permission from ref [132]. Copyright 2021 Science Advances.

4.3.2 TES-ADT

The effect of the simultaneous presence of at least two isomers on the kinetic fragility was studied. Two different isomers; *syn* TES-ADT and *anti* TES-ADT, as well as the mixture of these two, were investigated (see molecular structures in Figure 4.7a). *Anti* TES-ADT crystallized when cooled at a rate of less than -10 K s^{-1}, while *syn* TES-ADT crystallized at a rate of less than -50 K s^{-1}. Rapidly cooled material formed glassy films, suggesting a critical cooling rate of $q_{critical}$ = -10 K s^{-1} for *anti* TES-ADT and $q_{critical}$ = -50 K s^{-1} for *syn* TES-ADT (Figure 4.7b). The measured fragility was high for both materials, m = 174 and m = 136 for *anti* and *syn* TES-ADT, respectively. Therefore, both blends are fragile and can be classified as poor glass formers. Instead, the mixture displayed an excellent ability to form a stable molecular glass, resulting in a low fragility of only m = 27 (Figure 4.7b). The low kinetic fragility is likely due to the formation of mixed aggregates that stabilize the liquid

state, as reorganization requires collective motion of many molecules. Interestingly, similar to octonary perylene mixtures, two regimes with different slopes appear, in the plot of $-\log|q|$ vs. $T'_{f,ref}\ /T'_f$, for fast and slow cooling, respectively, suggesting a liquid-liquid transition when cooling at low rates (Figure 4.7b, c.f. 4.3.1 Perylene mixtures).

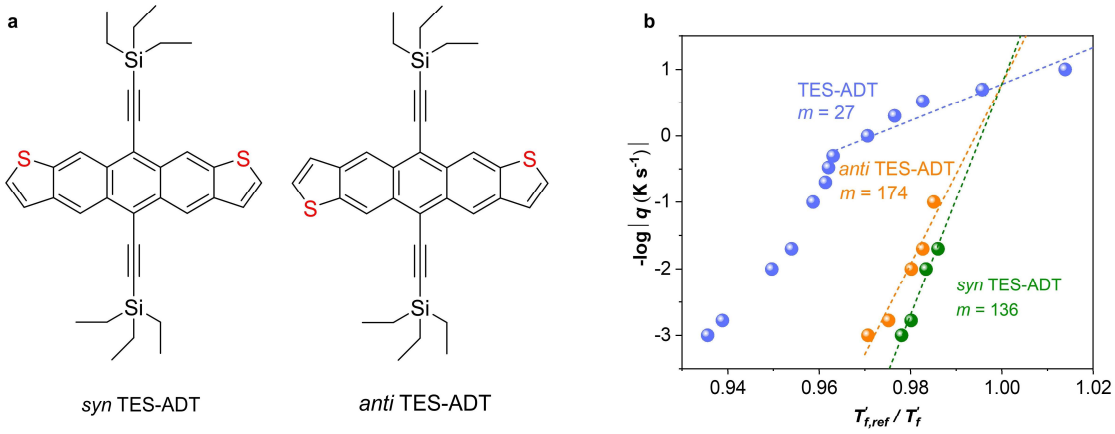

Figure 4.7. a) Molecular structures of *syn* TES-ADT and *anti* TES-ADT. b) Fragility plot of *anti* TES-ADT, syn TES-ADT and the mixture of these two. $T_{f,ref}$ = 27 °C measured with DSC.[139] The dotted lines are straight-line fits intersecting $T'_{f,ref} = T'_f$.

To verify the occurrence of a liquid-liquid transition, PL was utilized. The emission spectra observed after fast cooling from 150 °C to 25 °C at a rate of around -80 K s^{-1} revealed a peak at 570 nm, indicating the presence of monomers, and the peaks at lower energies were assigned to aggregates. Emission spectra after slow cooling at a rate of -0.1 K s^{-1} displayed only the aggregated state, in agreement with the occurrence of a liquid-liquid transition inferred from FSC (Figure 4.8). It should be noted that, DSC first heating scans of the mixture revealed a melting peak at around 140 °C and slow crystallization at $T_g < T < T_m$ has been described previously.[140] This indicates that the TES-ADT mixture still tends to crystallize despite its low fragility, and further investigation of the crystallization process is required.

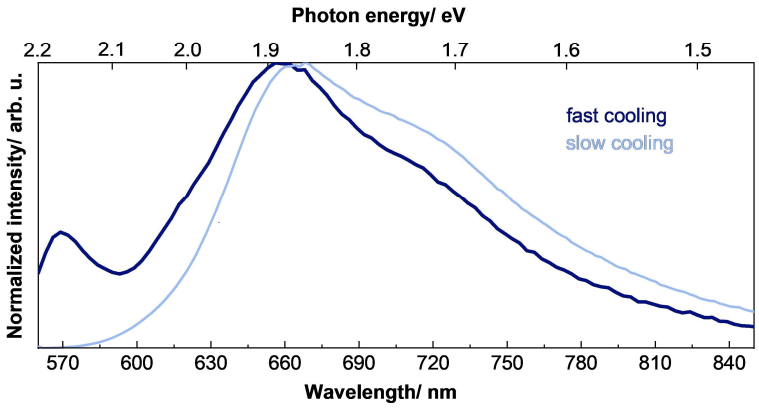

Figure 4.8 Emission spectra at 25 °C of the TES-ADT mixture after fast cooling at -80 K s^{-1} (dark blue) and slow cooling at -0.1 K s^{-1} (light blue).

4.3.3 P($g_4$2T-T):H-TFSI

The impact of doping on *m* was determined by investigating the polythiophene p($g_4$2T-T) co-processed with H-TFSI (Figure 4.9a). It was found that *m* decreases with H-TFSI concentration with the lowest values observed for the most strongly oxidized samples (Figure 4.9b). This suggests that oxidized p($g_4$2T-T) is a stronger glass former than neat p($g_4$2T-T). The decrease in fragility was attributed to the positive interactions between H-TFSI anions and the oligoether side chains and/or the positively charged backbone, which restricts the movement of oxidized polymer chains. Consequently, the reduced ability to undergo conformational changes may lead to a decreased ability to crystallize. This observation is supported by the lower degree of crystalline order indicated by GIWAXS diffractograms of highly doped films (Figure 2a, Paper II).[141]

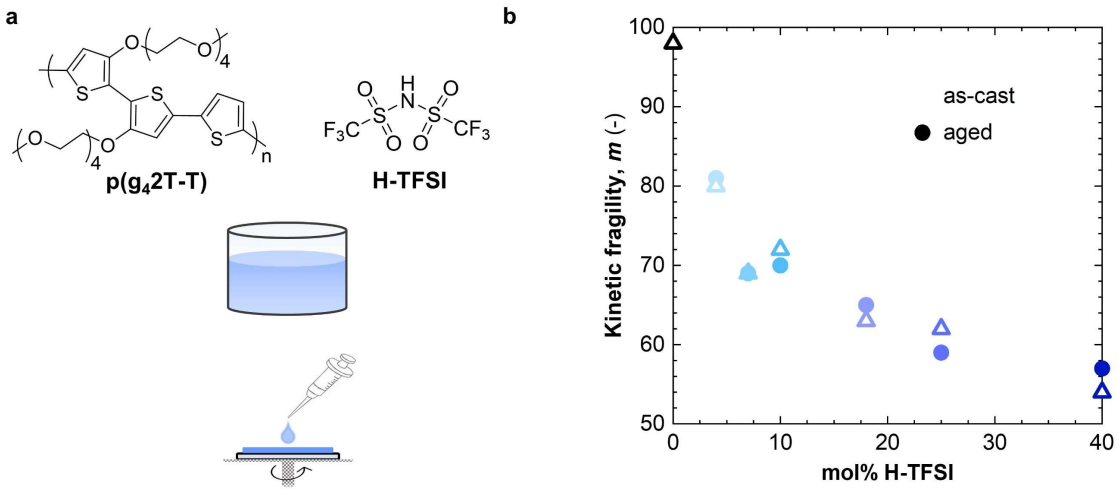

Figure 4.9. a) Molecular structures of p(g4 2T-T) and H-TFSI. b) Kinetic fragility vs mol% of H-TFSI. Adapted with permission from ref [141]. Copyright 2022 Royal Society of Chemistry.

4.3.4 Y-series acceptor mixtures

After learning that for some systems *m* decreases with mixing, the concept of mixing was used to investigate the stability of BHJs comprising acceptor mixtures. DSC was used to study the thermal behavior of the Y-series acceptors Y1, Y6, Y11, Y16, Y18 and the donor polymer PM6 (Figure 2.1 and 4.10). For the polymer PM6, no transitions were observed in DSC first heating scans (Figure 4.11). Instead, Y1 and Y6 display a crystallization exotherm above 220 °C, followed by a melting endotherm above 290 °C. Since the crystallization enthalpy is smaller than the melting enthalpy ($\Delta H_c < \Delta H_m$), it was proposed that Y1 and Y6 have a certain degree of order when cast from chloroform followed by further crystallization above 220 °C. Furthermore, Y11, Y16 and Y18 have only one endothermic peak above 280 °C indicating melting of an ordered phase that had formed during solidification. The acceptor mixtures Y6:Y11:Y16 and Y1:Y6:Y11:Y16:Y18 reveal melting peaks with a lower ΔH_m compared with neat acceptors and at lower temperatures, with T_m = 282 °C and T_m = 256 °C, respectively. The absence of melting endotherms above 280 °C for the blends Y1:Y6:Y11:Y16:Y18 and Y6:Y11:Y16 suggests that crystallization is strongly suppressed (Figure 4.11). The remaining broad endotherm may arise because crystallites are still present, which are however smaller in size or because co-crystals may have formed.

FSC thermograms could not be recorded for any of the individual acceptors when cooled with q = -1000 K s^{-1} or slower, probably because the critical cooling rate, $q_{critical}$, required to reach a glassy state is greater than -1000 K s^{-1}.[123] The Y6:Y11:Y16 blend cooled at low rates of less than -5 K s^{-1} crystallize. Instead, rapidly cooled material formed glassy films suggesting a critical cooling rate of $q_{critical}$ = -5 K s^{-1}. The pentanary acceptor mixture Y1:Y6:Y11:Y16:Y18 formed a glassy film at any cooling rate (Figure 4.11). The fragility was found to be m = 112 for Y1:Y6:Y11:Y16:Y18 and m = 195 for Y6:Y11:Y16. Therefore, both blends are fragile and can thus be classified as poor glass formers, which can be expected to crystallize if given sufficient time, consistent with the melting endotherms observed with DSC and the ordered phase indicated by GIWAXS (Figure 3, Paper I).[142]

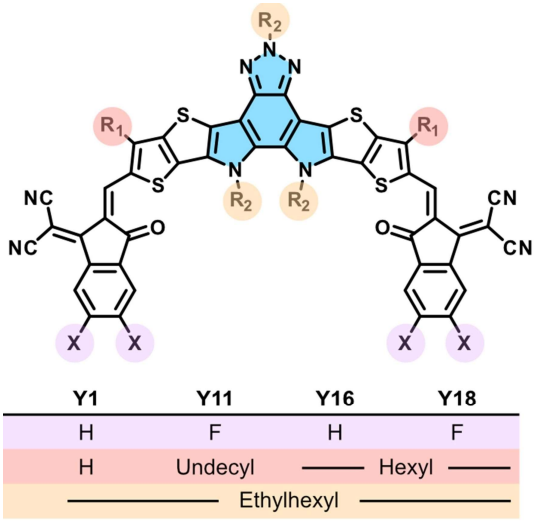

Figure 4.10. Chemical structures of Y1, Y11, Y16 and Y18. Adapted with permission from ref [142]. Copyright 2023 Springer Nature.

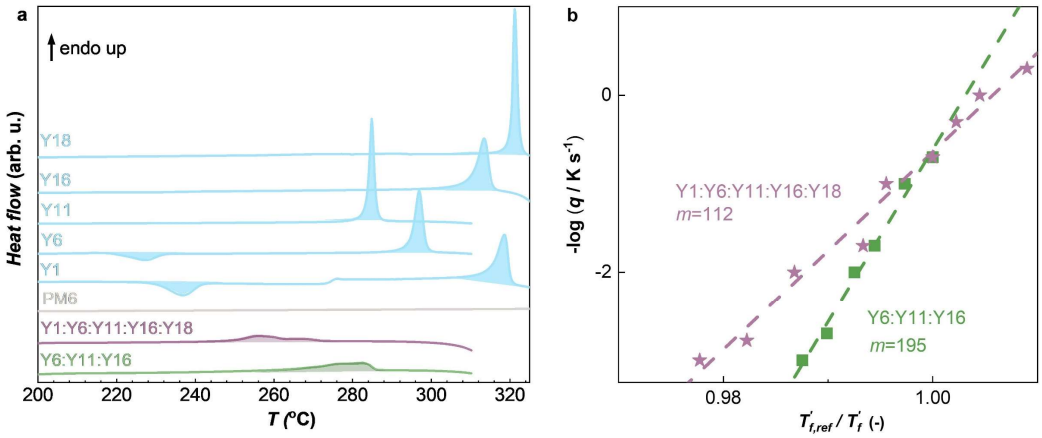

Figure 4.11. a) DSC first heating thermograms of Y18, Y16, Y11, Y6, Y1, PM6, Y1:Y6:Y11:Y16:Y18 and Y6:Y11:Y16. b) Fragility plot with -log|q| vs $T'_{f,ref}/T'_f$ with $T'_{f,ref}$ from FSC at 5 K s^{-1} for Y1:Y6:Y11:Y16:Y18 (purple) and Y6:Y11:Y16 (green). Adapted with permission from ref [142]. Copyright 2023 Springer Nature.

4.4 What does kinetic fragility mean for the field of OSCs?

To determine whether a material is a strong glass former and can be used for the fabrication of stable OSCs, three essential processes must be considered: 1) dissociation of aggregates, 2) phase separation, and 3) crystallization, as shown in Figure 4.11. Each of these processes contributes to the energy barrier necessary to prevent crystallization. There is an energy barrier to separate different molecules in mixed aggregates so that they can assemble again but with the same type of molecule. Phase separation has an energy barrier if it occurs via binodal decomposition and crystallization has an energy barrier as work is required to form a nucleus of critical size. Some multicomponent systems, for example the octonary perylene mixture discussed in chapter 4.3.1, have a high energy barrier to crystallization because of contributions from all three processes 1-3. The material therefore displays an unprecedented ability to form a stable molecular glass with a very low kinetic fragility. Y-series derivative mixtures, on the other hand, do not show a liquid-liquid transition in their Angell plot (c.f. Figure 4.10b), and therefore do not form mixed aggregates. They have an energy barrier with contributions from the phase separation and crystallization process and therefore the kinetic fragility is high.

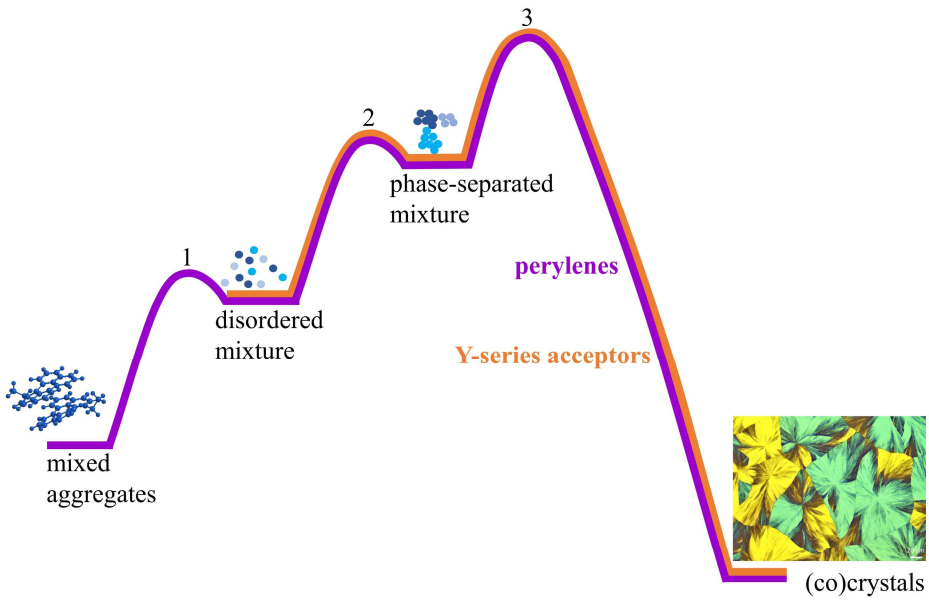

Figure 4.11. Energy barrier to crystallization for perylenes (purple) and Y-series acceptors (orange) with contributions from (1) dissociation of aggregates (2) phase separation, and (3) crystallization**.**

5 Stability of photovoltaic devices

The efficiency of lab-scale devices is approaching 20 %.[17-20] However, devices with a projected stability of at least 20 years have not yet been achieved. Improving stability is a prerequisite for making them commercially viable. Printing of OSCs is typically done at temperatures up to 140 ℃ to enable fast solvent evaporation.[22-23] Printing of the hole transport layer requires similar temperatures and the solar cell also experience heat during operation, causing many OSCs to coarsen, which often degrades the solar cell performance.[24-25] Usually, the optimal active layer nanostructure that results in the highest efficiency is not in thermal equilibrium and thus evolves with time, especially at elevated temperatures. Therefore, understanding the different degradation mechanisms of OSCs is essential for improving their thermal stability. In the following chapters, different degradation mechanisms of OSCs will be discussed, as well as the strategy of mixing several acceptors to improve the thermal stability of OSCs.

5.1 Different degradation mechanisms of OSCs

Different degradation mechanisms can occur depending on different triggers such as heat, light, oxygen, water, and mechanical stress, which can lead to a decrease in the solar cell performance over time. For instance, oxygen and water can diffuse into the device and cause physical and chemical degradation. Oxidation reactions on the metal electrodes can result in the formation of metal oxides, creating an electrically insulating layer that hinders charge transport and extraction.[143] Defects can also arise between the electrodes and the carrier transport layers, which act as pinholes.[144-146] The carrier transport layer, and the active layer can also experience degradation. For example, PEDOT:PSS can exhibit acidity leading to corrosion of the electrode, and the active layer can undergo radical reduction reactions.[147-148] The presence of light and oxygen can cause photochemical and photophysical degradation by oxidizing the active layer, resulting in changes in the structures of the donor and acceptor molecules.[149] Additionally, radical-based reactions of the active layer can lead to photo-bleaching.[150] Heat can affect the photovoltaic performance in different ways. At elevated temperatures, the active layer can undergo phase separation and crystallization (see 3.1 Phase separation and crystallization in BHJ blends and 3.2 Interplay of T_g and nanostructure stability). This evolution of the active

layer can reduce its adhesion to the carrier transport layer and impede electron extraction.[151] Elevated temperatures can also promote diffusion of metal atoms from the electrodes into the active layer.[152-154] Furthermore, mechanical stress can change the nanostructure or cause delamination of the different layers in the device.[155] Intrinsic degradation, which refers to degradation without any external triggers, can occur due to changes in the nanostructure of the active layer or the diffusion of molecules from the carrier transport layer or electrodes.[144, 156-159] The diffusion of atoms can modify the energy levels of the device layers or create traps in the active layer, leading to charge recombination.[149]

Various strategies have been developed to mitigate degradation mechanisms. For instance, encapsulation with a UV-filter to protect the device from oxygen, water, and high-energy photons.[160] Additionally, the addition of antioxidants can suppress formation of radicals.[161] Another approach involves arresting the evolution of the BHJ nanostructure by using mixtures and high T_g materials (see 3.3 Vitrification of phases) which has been the focus of this thesis.

5.2 Thermal stability and photovoltaic performance

The evolution of the active layer nanostructure occurs over time, and heating accelerates this development and provides information about what can happen over longer periods of time at lower temperatures. To determine the suitability of OSCs for large-scale manufacturing, it is necessary to study how the nanostructure of the active layer can withstand elevated temperatures. In the following sections, mixing of acceptors as a tool to improve the stability of the active layer nanostructure is discussed. OSCs of blends comprising ITIC-series or Y6-series acceptors were subjected to thermal annealing at different temperatures and the photovoltaic performance was measured to investigate the effect of mixing on the thermal stability.

5.2.1 ITIC-series ternary devices

Two acceptors, ITIC-4F and ITIC-4Cl, were studied due to their structural similarities (see Figure 2.1 for chemical structures). DSC was used to construct a phase diagram of the mixture of these two acceptors. The DSC heating thermograms displayed a melting peak at 155 °C for ITIC-4F and 180 °C for ITIC-4Cl, while the 1:1 mixture of ITIC-4F:ITIC-4Cl exhibited a melting peak at 160 °C (Figure 5.1a,b). This suggests that ITIC-4F and ITIC-4Cl interact with each other, potentially forming co-crystals. GIWAXS measurements confirmed the co-crystallization of the 1:1 ITIC-4F:ITIC-4Cl mixture, as a shift in peak position was observed compared to the pristine acceptor material (Figure 5.1c). The co-crystallization is likely facilitated by halogen interactions between fluorine and chlorine, which aid in aligning the two acceptors within the same crystal lattice. Acceptor molecules that have not joined a crystal instead form an amorphous mixture driven by an increase in ΔS_{mix} as well as a more negative ΔH_{mix} (assuming that F···Cl interactions persist in the disordered state).[49]

The phase behavior of 1:1 ITIC 4F:ITIC-4Cl was investigated after the addition of the donor polymer PTB7-Th. A blend ratio of 1:0.5:0.5 (wt%) PTB7-Th:ITIC-4F:ITIC-4Cl was studied, which also gave the best solar cell performance. Diffraction patterns of the cast ternary mixture, as well as films annealed at 160 °C have only a broad amorphous halo around $q \approx 17$ nm^{-1}, suggesting that the presence of the polymer effectively suppressed the co-crystallization of the acceptor mixture.

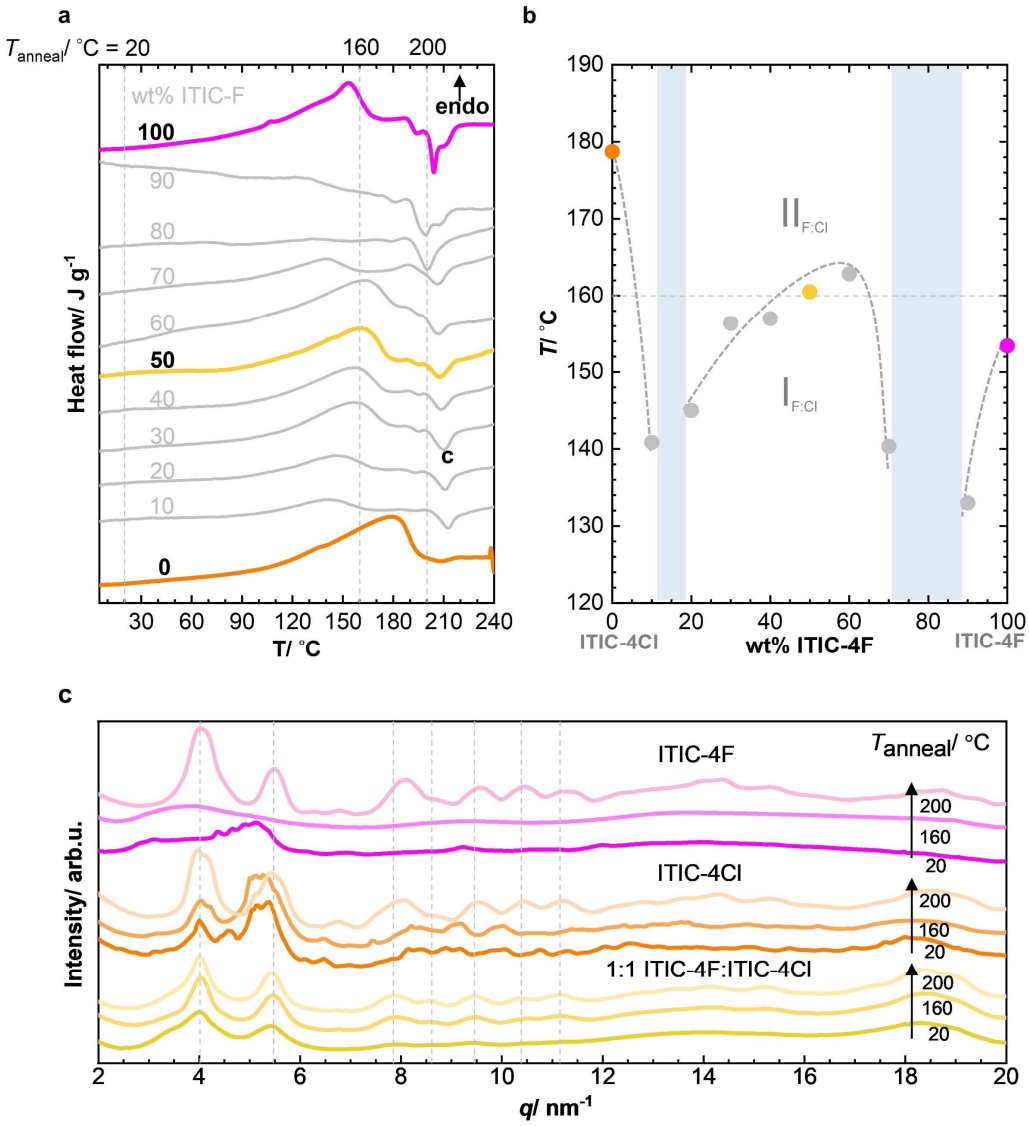

Figure 5.1. a) DSC first heating thermograms of ITIC-4F and ITIC-4Cl and various mixtures of these two. b) Phase diagram showing the change in endothermic peak position of ITIC-4F:ITIC-4Cl measured by DSC. c) GIWAXS diffractograms of ITIC-4F, ITIC-4Cl and 1:1 ITIC-4F:ITIC-4Cl after annealing at 20, 160 or 200 °C. Adapted with permission from ref [49]. Copyright 2020 Wiley.

In a further set of experiments, atomic force microscopy based infrared spectroscopy (AFM-IR) was used. AFM-IR combines chemical analysis by infrared spectroscopy with structure analysis by atomic force microscopy. In AFM-IR, pulses of laser radiation hit the AFM cantilever, which is in contact with the material, causing thermal expansion. The fast and short-lived expansion stimulates resonant oscillation of the AFM cantilever. The cantilever oscillation amplitude is proportional to the absorption coefficient of the material. By varying the IR frequency and keeping the cantilever at the same position, an absorption spectrum can be measured, providing a unique fingerprint of the nanoscale region. A map with areas enriched in a specific chemical compound can be obtained by keeping the same IR frequency while moving the cantilever around the surface.[162]

AFM-IR was used to compare the blend nanostructures of the binaries 1:1 PTB7-Th:ITIC-4F, 1:1 PTB7-Th:ITIC-4Cl with the ternary 1:0.5:0.5 PTB7-Th:ITIC-4F:ITIC-4Cl. The IR spectra of pure ITIC-4F and ITIC-4Cl show peaks unique for each material i.e. 1345 cm^{-1} for ITIC-4F and 1572 cm^{-1} for ITIC-4Cl while both acceptors absorb at 1280 cm^{-1} (Figure 5.2a). When imaging samples at 1280 cm^{-1} after annealing at 160 °C, crystals protruding 50-60 nm from the surface were observed in the two binaries while no crystals were observed in the ternary (Figure 5.2c,d).

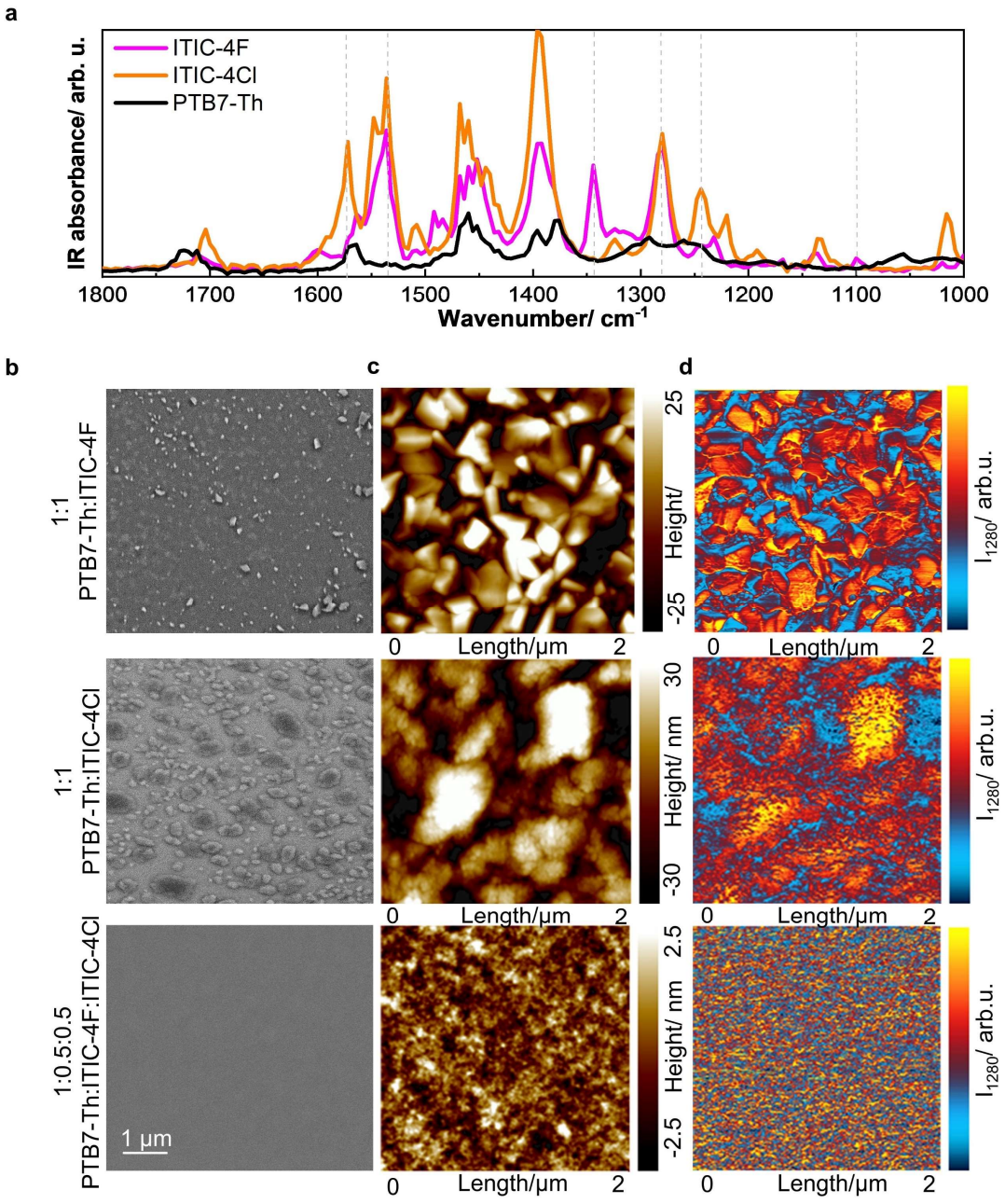

Figure 5.2. a) FTIR spectra for the neat films of ITIC-4F, ITIC-4Cl and PTB7-Th. b) SEM , c) AFM and d) AFM-IR images recorded at 1280 cm^{-1} of 1:1 PTB7-Th:ITIC-4F, 1:1 PTB7-Th:ITIC-4Cl and 1:0.5:0.5 PTB7-Th:ITIC-4F:ITIC-4Cl. Adapted with permission from ref [49]. Copyright 2020 Wiley.

AFM-IR was also used to map the acceptors. The film was imaged using 1345 cm^{-1} to map ITIC-4F (Figure 5.3b) and 1572 cm^{-1} to map ITIC-4Cl (Figure 5.3c). The two AFM-IR images reveal acceptor domains with the same shape, indicating that both acceptors absorb at the same location within the ternary film, surrounded by polymer domains.

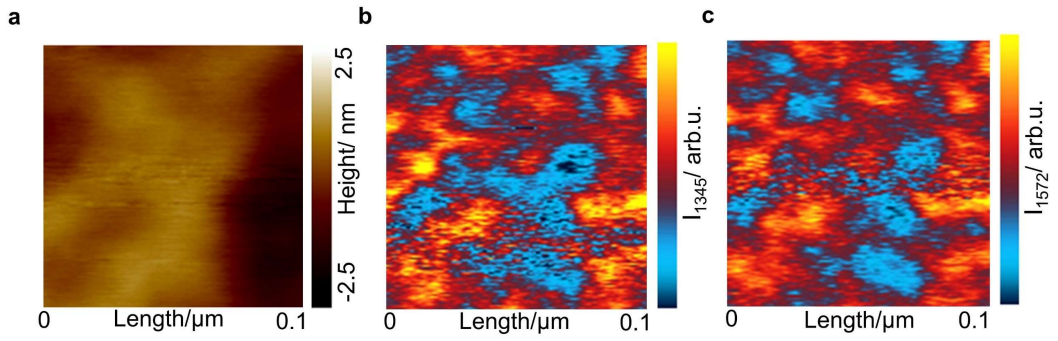

Figure 5.3. The same area of 1:0.5:0.5 PTB7-Th:ITIC-4F:ITIC-4Cl recorded a) in height mode b) at 1345 cm^{-1} where only ITIC-4F absorbs or c) at 1572 cm^{-1} where only ITIC-4Cl absorbs. Adapted with permission from ref [49]. Copyright 2020 Wiley.

The thermal stability of the ternary 1:0.5:0.5 PTB7-Th:ITIC-4F:ITIC-4Cl was compared to the two binaries 1:1 PTB7-Th:ITIC-4F and 1:1 PTB7-Th:ITIC-4Cl. The active layers were annealed at temperatures ranging from 25-200 ºC for 10 minutes before evaporation of the MoOx interlayer and Ag electrodes. At 150 ºC, the ternary remains stable, while a 10% decrease in PCE can be observed for PTB7-Th:ITIC-4F and a 20% decrease for PTB7-Th:ITIC-4Cl (Figure 5.4a). This is due to the suppressed crystallization in case of the ternary compared to the two binaries, which experience crystallization of the acceptors.

In another experiment, the active layers were annealed at 130 ℃ for up to 205 hours to investigate the thermal stability during longer annealing times (Figure 5.4b). Binary devices undergo burn-in during the first 50-70 hours, resulting in a reduction in efficiency by at least a third. Impressively, due to a more stable nanostructure of the ternary, the burn-in was avoided and the efficiency remained stable at least 205 hours. This indicates that the ternary offers good thermal stability. Hence, device manufacturing and operation at high temperatures can be considered.

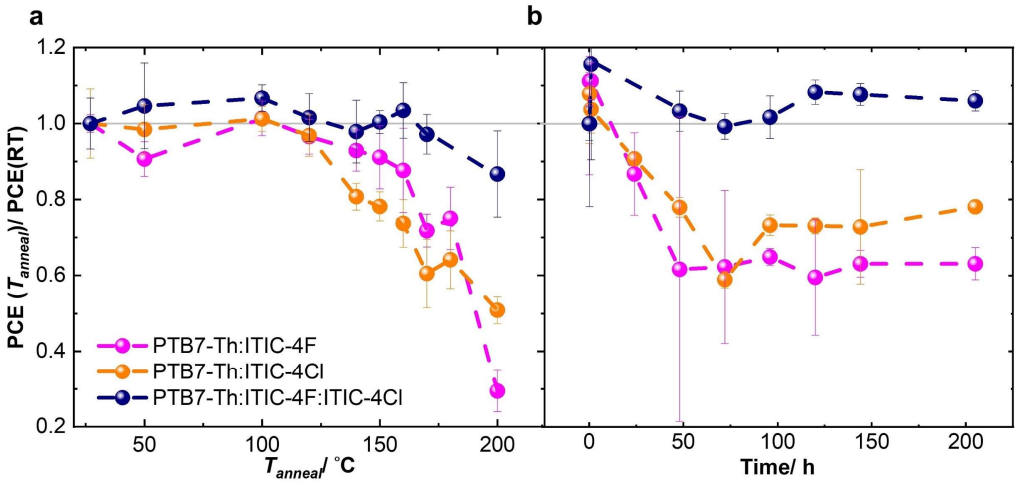

Figure 5.4. PCE of PTB7-Th:ITIC-4F, PTB7-Th:ITIC-4Cl and PTB7-Th:ITIC-4F:ITIC-4Cl a) for samples annealed at 25-200 ºC for 10 minutes at each temperature b) for samples annealed at 130 ºC up to 205 hours. Adapted with permission from ref [49]. Copyright 2020 Wiley. Sri Harish Kumar Paleti collected all the device data at KAUST.

5.2.2 Y-series hexanary devices

Y-series acceptor mixtures were investigated to explore the effect on the thermal stability of OSCs. The Y-series acceptors Y1, Y6, Y11, Y16, Y18 with similar LUMO levels were chosen for this study together with the donor polymer PM6 (see chemical structures in Figure 2.1 and Figure 1 in Paper I).

GIWAXS measurements of the binary PM6:Y6 and the hexanary PM6:Y1:Y6:Y11:Y16:Y18 showed diffraction patterns of the donor PM6, indicating that the donor has phase separated into polymer-rich domains. AFM-IR was used to validate the presence of polymer- and acceptor- rich regions in the hexanary. IR spectra of neat films of the acceptor and donor materials featured unique peak for PM6 at 1648 cm^{-1} arising from alkene vibrations (Figure 5.5). This wavenumber was used to map areas enriched with PM6. A homogenous phase with

small donor-rich regions of 10 to 100 nm protruding only about 5 nm from the surface was observed, probably surrounded by acceptor-rich regions (Figure 5.5).

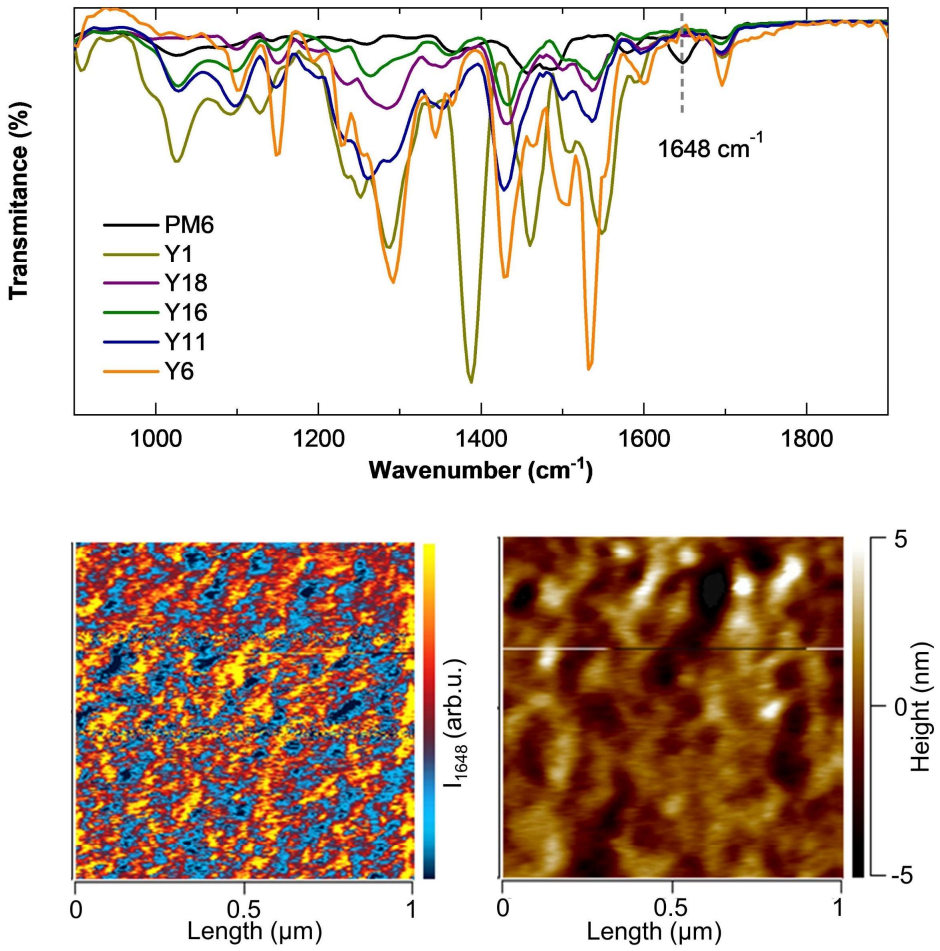

Figure 5.5. FTIR spectra for neat films of PM6, Y1, Y6, Y11, Y16 and Y18. AFM-IR image of PM6:Y1:Y6:Y11:Y16:Y18 recorded at 1648 cm^{-1} and AFM in height mode. Adapted with permission from ref [142]. Copyright 2023 Springer Nature.

The thermal stability upon longer annealing times of hexanary blends was compared with binary blends. The active layers were annealed at 130 ℃ for 23 days before spin-coating of the electron transport layer and evaporation of the electrode. The efficiency of binary devices decreased by about a third from the initial value, mainly due to a decrease in FF. Impressively, due to a more stable nanostructure, the efficiency of the hexanary device was

stable even after 23 days of ageing (Figure 5.6). This indicates that the photovoltaic performance of hexanary blends are thermally stable and high-throughput device fabrication at elevated temperatures up to 130 ℃ can be considered.

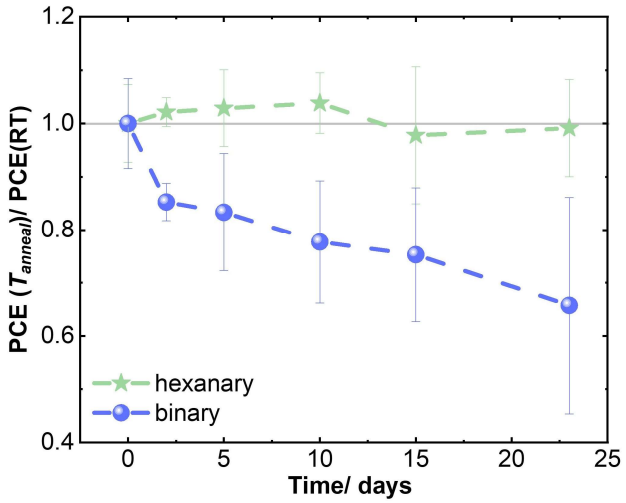

Figure 5.6. PCE of PM6:Y1:Y6:Y11:Y16:Y18 and PM6:Y6 devices annealed at 130 ℃ as compared to the initial PCE of as-cast devices. Adapted with permission from ref [142]. Copyright 2023 Springer Nature. Sri Harish Kumar Paleti collected all the device data at KAUST.

6 Conclusions

Organic solar cells are a promising renewable alternative energy source with numerous advantages. They promise, for example, scalability through printing or coating techniques, a short energy pay-back time, light weight, semi-transparency, and flexibility. However, high-throughput printing techniques require at least one heating step, and the solar cells experience heat during operation. The optimal nanostructure of the active layer typically deviates from thermodynamic equilibrium and evolves over time, especially at elevated temperatures, leading to device performance degradation. The focus of this thesis has been on improving the thermal stability of the active layer nanostructure.

The initial part of the thesis investigated the impact of mixing on glass formation. To gain a better understanding of how mixing influences glass formation, a model system consisting of up to eight different perylene derivatives was developed. The results revealed that the octonary perylene mixture exhibited an unprecedented ability to form a stable molecular glass, assigned to a high energy barrier that prevents crystallization. The exceptional tendency for vitrification could be attributed to the formation of aggregates that stabilize the liquid state. Next, the thesis investigated the simultaneous presence of two isomers on glass formation using the small molecule semiconductor TES-ADT. Binary mixtures of isomers also formed mixed aggregates that stabilize the liquid state, as reorganization requires collective motion of many molecules. Furthermore, the thesis examined the effect of doping on glass formation by analyzing blends of polythiophene p($g_4$2T-T) and the bistriflimidic acid H-TFSI. The blends showed a strong tendency for glass formation, which was attributed to the restricted motion of oxidized polymer chains caused by positive interactions between H-TFSI anions and the oligoether side chains and/or the positively charged backbone. Additionally, the thesis analyzed organic photovoltaic acceptor mixtures to investigate their impact on crystallization and glass formation. It was found that binary mixtures of ITIC series acceptors co-crystallized, while mixtures of three to five derivatives from the Y series exhibited a significantly reduced tendency for crystallization compared to neat materials, although small crystals or co-crystals were still present.

The thesis then discussed the use of acceptor mixtures to improve the thermal stability of organic photovoltaic devices. Ternary solar cell devices consisting of two ITIC series acceptors and one donor were fabricated. The polymer suppressed co-crystallization of the two acceptors, and hence the ternary blend demonstrated a highly stable nanostructure. This resulted in a significantly improved thermal stability compared to the binary blends, which suffered from acceptor crystallization. The device performance of the ternary blend remained stable even when annealed at temperatures up to 170 ºC. Finally, the thesis also discussed hexanary blends composed of five different Y-series acceptor molecules and one donor polymer. Remarkably, the efficiency of hexanary devices remained stable even after the active layer was subjected to 23 days of ageing at 130 ºC. This suggests that by mixing several acceptors, it is possible to create thermally stable materials and devices so that processing and operation at high temperatures can be considered.

7 Outlook

The results of this thesis are expected to have relevance beyond the mixtures examined here. Consequently, this thesis is likely to inspire further investigations into semiconductor mixtures. The thesis provides some design guidelines for stable mixtures, with one example being the requirement for molecules to possess a certain degree of differentiation to yield the desired increase in entropy upon mixing. Mixtures of differently halogenated molecules or blends of isomers appear to provide sufficient differentiation to achieve a higher entropy of mixing. However, mixing perylene with deuterated perylene, for instance, did not produce any discernible effect. This suggests that deuteration may not induce a significant enough change in the molecular structure. The thesis also suggests that some molecules interact and form mixed aggregates. Using modelling to identify molecules capable of forming aggregates may be a promising approach to uncover stable mixtures that do not crystallize.

Additionally, accelerated ageing studies to evaluate the impact of vitrification after prolonged periods is important to judge long term stability. Measuring the associated fragility of physical vapor deposited samples could provide valuable insight into the effects of aging. Investigating the kinetic fragility of films with different thicknesses could also yield interesting results, as different thicknesses can affect the T_g. Furthermore, it would be interesting to combinate FSC with light soaking experiments because of the structural changes that are likely induced by photoexcitation and their impact on glass formation. Investigating how conjugated polymers adopt different conformations upon light absorption would be a further avenue for investigation.

Moreover, utilizing SEM together with focused ion beam to cut out a cross-section of a solar cell device and examine its cross-section using AFM-IR, SEM-EDX or Raman spectroscopy could provide insights into the interplay between different layers and phase separation/crystallization in the bulk of the active layer. Finally, rheometry could be used to confirm fragility values. The viscosity profile of mixtures may provide information about interactions between acceptors and donors. Some donor: acceptor systems form a gel in the processing solvent, and the rheometer can monitor the viscosity of the gel during heating/cooling to investigate when the gel dissociates. In conclusion, this thesis will hopefully inspire new project ideas and provide new insights into semiconductor mixtures.

8 Acknowledgement

First, I would like to express my gratitude to my main supervisor Christian Müller for giving me this opportunity to pursue a PhD and for guiding and supporting me in all my projects. I have enjoyed being a part of your group and all the discussions we have had during this time.

I would like to thank my examiner Kasper Moth-Poulsen and all my colleagues on floor 8 and the Müller group for all the discussions and the fun times. I would also like to thank my co-supervisor Ellen Moons and all my colleagues in Karlstad for supporting me and for giving me the warmest welcome every time I visit Karlstad. Thank you, Ishita Jalan, Jan Van Stam and Leif Ericsson, for sharing the coolest adventure together with me! It has been so much fun collaborating with you! Thank you Sozan Darabi for the 10 years of friendship together at Chalmers!

Thanks to all my collaborators that have contributed to this work. Especially, thanks to Derya Baran, Sri Harish Kumar Paleti, Liyang Yu, Clara Schäfer, Alex Cravcenco, Karl Börjesson, Paul Erhart, Furqan Farooqi, Yanfeng Liu, Jonas Berqvist, Fengling Zhang, Donghyun Kim, Igor Zozoulenko, Ferry Anggoro Ardy Nugroho, Albert Harillo, Fengling Zhang, Cristoph Langhammer, John E. Anthony and Mariano Campoy-Quiles.

Thank you Sara Marina and Jaime Martín for teaching me how to use FSC and for showing me all the good tapas in San Sebastián!

Last but not least, thank you my beloved parents Catherine and Göran, my siblings Marcus and Louisa, my parents-in-law Rustan and Ann-Margret, Maja, Casper, Anton and Sofie for all your love, support and belief in me.

9 References

[1] M. R. a. P. R. Hannah Ritchie, Energy, http://ourworldindata.org/energy, accessed: 2023-09-27.

[2] Eia, International energy outlook, https://www.eia.gov/outlooks/ieo/, accessed: 2023-10-05.

[3] Eurostat, Renewable energy statistics, http://ec.europa.eu/eurostat/statistics-explained/index.php?title=Renewable_energy_statistics, accessed: 2023-09-27.

[4] EPA, What is acid rain?, https://www.epa.gov/acidrain/what-acid-rain, accessed: 2023-09-29.

[5] UNFCCC, http://unfccc.int/process-and-meetings/the-paris-agreement, accessed: 2023-09-27.

[6] F. Birol, The global energy crisis highlights the need for a massive surge in clean energy investment, http://imf.org/en/Publications/fandd/issues/2022/12/a-call-to-clean-energy-fatih-birol, accessed: 2023-09-27.

[7] Share of energy consumption from renewable sources in Europe (8th EAP), http://eea.europa.eu/ims/share-of-energy-consumption-from, accessed: 2023-09-27.

[8] NREL, Solar Energy Basics, https://www.nrel.gov/research/re-solar.html, accessed: 2023-09-29.

[9] J. Yoon, Y. Sun, J. A. Rogers, in *Semiconductor Nanomaterials for Flexible Technologies*, DOI: https://doi.org/10.1016/B978-1-4377-7823-6.00006-4 (Eds: Y. Sun, J. A. Rogers), William Andrew Publishing, Oxford **2010**, p. 159.

[10] D. M. Chapin, C. S. Fuller, G. L. Pearson, *J. Appl. Phys.* **2004**, 25, 676.

[11] M. A. Green, Y. Hishikawa, E. D. Dunlop, D. H. Levi, J. Hohl-Ebinger, A. W. Y. Ho-Baillie, *Prog. Photovolt.: Res. Appl.* **2018**, 26, 427.

[12] K. Yoshikawa, H. Kawasaki, W. Yoshida, T. Irie, K. Konishi, K. Nakano, T. Uto, D. Adachi, M. Kanematsu, H. Uzu, K. Yamamoto, *Nat. Energy* **2017**, 2, 17032.

[13] A. Galimshina, A. Hollberg, J. McCarty, C. Waibel, A. Schlueter, *IOP Conf.* **2023**, 1196, 012014.

[14] D. Govindarajan, K. K. Chinnakutti, in *Oxide Free Nanomaterials for Energy Storage and Conversion Applications*, DOI: https://doi.org/10.1016/B978-0-12-823936-0.00010-3 (Eds: P. Arunachalam, J. Theerthagiri, A. M. Al-Mayouf, M. Y. Choi, M. Jagannathan), Elsevier **2022**, p. 51.

[15] R. A. Senthil, J. Theerthagiri, S. K. K. Pasha, M. Jagannathan, A. N. Grace, S. Manickam, in *Oxide Free Nanomaterials for Energy Storage and Conversion Applications*, DOI: https://doi.org/10.1016/B978-0-12-823936-0.00009-7 (Eds: P. Arunachalam, J. Theerthagiri, A. M. Al-Mayouf, M. Y. Choi, M. Jagannathan), Elsevier **2022**, p. 307.

[16] M. Ebrahimi, in *Power Generation Technologies*, DOI: https://doi.org/10.1016/B978-0-323-95370-2.00010-7 (Ed: M. Ebrahimi), Academic Press **2023**, p. 419.

[17] T. Chen, S. Li, Y. Li, Z. Chen, H. Wu, Y. Lin, Y. Gao, M. Wang, G. Ding, J. Min, Z. Ma, H. Zhu, L. Zuo, H. Chen, *Adv. Mater.* **2023**, 35, 2300400.

[18] J. Wang, Z. Zheng, Y. Zu, Y. Wang, X. Liu, S. Zhang, M. Zhang, J. Hou, *Adv. Mater.* **2021**, 33, 2102787.

[19] Y. Cui, H. Yao, J. Zhang, K. Xian, T. Zhang, L. Hong, Y. Wang, Y. Xu, K. Ma, C. An, C. He, Z. Wei, F. Gao, J. Hou, *Adv. Mater.* **2020**, 32, 1908205.

[20] K. Jiang, J. Zhang, C. Zhong, F. R. Lin, F. Qi, Q. Li, Z. Peng, W. Kaminsky, S.-H. Jang, J. Yu, X. Deng, H. Hu, D. Shen, F. Gao, H. Ade, M. Xiao, C. Zhang, A. K. Y. Jen, *Nat. Energy* **2022**, 7, 1076.

[21] Cutting edge indoor solar cells, http://epishine.com, accessed: 2023-09-27.

[22] M. Jørgensen, K. Norrman, S. A. Gevorgyan, T. Tromholt, B. Andreasen, F. C. Krebs, *Adv. Mater.* **2012**, 24, 580.

[23] F. C. Krebs, *Sol. Energy Mater. Sol. Cells* **2009**, 93, 394.

[24] S. Strohm, F. Machui, S. Langner, P. Kubis, N. Gasparini, M. Salvador, I. McCulloch, H. J. Egelhaaf, C. J. Brabec, *Energy Environ. Sci.* **2018**, 11, 2225.

[25] E. Bihar, D. Corzo, T. C. Hidalgo, D. Rosas-Villalva, K. N. Salama, S. Inal, D. Baran, *Ad. Mater. Technol.* **2020**, 5, 2000226.

[26] W. U. Huynh, J. J. Dittmer, A. P. Alivisatos, *Science* **2002**, 295, 2425.

[27] C. J. Brabec, *Sol. Energy Mater. Sol. Cells* **2004**, 83, 273.

[28] Y. Li, *Acc. Chem. Res.* **2012**, 45, 723.

[29] J. Chen, Y. Cao, *Acc. Chem. Res.* **2009**, 42, 1709.

[30] M. Svensson, F. Zhang, S. C. Veenstra, W. J. H. Verhees, J. C. Hummelen, J. M. Kroon, O. Inganäs, M. R. Andersson, *Adv. Mater.* **2003**, 15, 988.

[31] E. E. Neuteboom, S. C. J. Meskers, P. A. van Hal, J. K. J. van Duren, E. W. Meijer, R. A. J. Janssen, H. Dupin, G. Pourtois, J. Cornil, R. Lazzaroni, J.-L. Brédas, D. Beljonne, *J. Am. Chem. Soc.* **2003**, 125, 8625.

[32] E. Bundgaard, F. C. Krebs, *Sol. Energy Mater. Sol. Cells* **2007**, 91, 954.

[33] Y. Sun, C. Cui, H. Wang, Y. Li, *Adv. Energy Mater.* **2012**, 2, 966.

[34] C. Yan, S. Barlow, Z. Wang, H. Yan, A. K. Y. Jen, S. R. Marder, X. Zhan, *Nat. Rev. Mater.* **2018**, 3, 18003.

[35] J. Hou, O. Inganäs, R. H. Friend, F. Gao, *Nat. Mater.* **2018**, 17, 119.

[36] Y. Lin, J. Wang, Z.-G. Zhang, H. Bai, Y. Li, D. Zhu, X. Zhan, *Adv. Mater.* **2015**, 27, 1170.

[37] J. Yuan, Y. Zhang, L. Zhou, G. Zhang, H.-L. Yip, T.-K. Lau, X. Lu, C. Zhu, H. Peng, P. A. Johnson, M. Leclerc, Y. Cao, J. Ulanski, Y. Li, Y. Zou, *Joule* **2019**, 3, 1140.

[38] S. Li, L. Ye, W. Zhao, S. Zhang, S. Mukherjee, H. Ade, J. Hou, *Adv. Mater.* **2016**, 28, 9423.

[39] J. Yuan, Y. Zou, *Org. Electron.* **2022**, 102, 106436.

[40] R. J. Ouellette, J. D. Rawn, in *Organic Chemistry Study Guide*, DOI: https://doi.org/10.1016/B978-0-12-801889-7.00001-7 (Eds: R. J. Ouellette, J. D. Rawn), Elsevier, Boston **2015**, p. 1.

[41] M. Manceau, E. Bundgaard, J. E. Carlé, O. Hagemann, M. Helgesen, R. Søndergaard, M. Jørgensen, F. C. Krebs, *J. Mater. Chem.* **2011**, 21, 4132.

[42] C. K. Chiang, C. R. Fincher, Y. W. Park, A. J. Heeger, H. Shirakawa, E. J. Louis, S. C. Gau, A. G. MacDiarmid, *Phys. Rev. Lett.* **1977**, 39, 1098.

[43] D. Chen, C. Zhang, Z. Wang, R. Gao, Y. Hao, *Differences of conventional and inverted organic solar cells in optical aspect*, **2012**.

[44] W. Yu, L. Huang, D. Yang, P. Fu, L. Zhou, J. Zhang, C. Li, *J. Mater. Chem. A* **2015**, 3, 10660.

[45] Z. Liang, Q. Zhang, O. Wiranwetchayan, J. Xi, Z. Yang, K. Park, C. Li, G. Cao, *Adv. Funct. Mater.* **2012**, 22, 2194.

[46] Y. Sun, G. C. Welch, W. L. Leong, C. J. Takacs, G. C. Bazan, A. J. Heeger, *Nat. Mater.* **2012**, 11, 44.

[47] M. Wang, Y. Li, H. Huang, E. D. Peterson, W. Nie, W. Zhou, W. Zeng, W. Huang, G. Fang, N. Sun, X. Zhao, D. L. Carroll, *Appl. Phys. Lett.* **2011**, 98.

[48] C. Girotto, E. Voroshazi, D. Cheyns, P. Heremans, B. P. Rand, *ACS Appl. Mater. Interfaces* **2011**, 3, 3244.

[49] S. Hultmark, S. H. K. Paleti, A. Harillo, S. Marina, F. A. A. Nugroho, Y. Liu, L. K. E. Ericsson, R. Li, J. Martín, J. Bergqvist, C. Langhammer, F. Zhang, L. Yu, M. Campoy-Quiles, E. Moons, D. Baran, C. Müller, *Adv. Funct. Mater.* **2020**, 30, 2005462.

[50] A. J. Heeger, *Adv. Mater.* **2014**, 26, 10.

[51] C. J. Brabec, G. Zerza, G. Cerullo, S. De Silvestri, S. Luzzati, J. C. Hummelen, S. Sariciftci, *Chem. Phys. Lett.* **2001**, 340, 232.

[52] N. Kaur, M. Singh, D. Pathak, T. Wagner, J. M. Nunzi, *Synth. Met.* **2014**, 190, 20.

[53] T.-H. Lai, S.-W. Tsang, J. R. Manders, S. Chen, F. So, *Mater. Today* **2013**, 16, 424.

[54] R. A. Street, M. Schoendorf, A. Roy, J. H. Lee, *Phys. Rev. B* **2010**, 81, 205307.

[55] J. D. Servaites, M. A. Ratner, T. J. Marks, *Energy Environ. Sci.* **2011**, 4, 4410.

[56] D. Credgington, F. C. Jamieson, B. Walker, T.-Q. Nguyen, J. R. Durrant, *Adv. Mater.* **2012**, 24, 2135.

[57] P. Blom, V. Mihailetchi, L. Koster, D. Markov, *Adv. Mater.* **2007**, 19, 1551.

[58] T. L. Benanti, D. Venkataraman, *Photosynth. Res.* **2006**, 87, 73.

[59] G. Yu, J. Gao, J. C. Hummelen, F. Wudl, A. J. Heeger, *Science* **1995**, 270, 1789.

[60] W. Ma, C. Yang, X. Gong, K. Lee, A. J. Heeger, *Adv. Funct. Mater.* **2005**, 15, 1617.

[61] K. Vandewal, K. Tvingstedt, A. Gadisa, O. Inganäs, J. V. Manca, *Nat. Mater.* **2009**, 8, 904.

[62] J. Benduhn, K. Tvingstedt, F. Piersimoni, S. Ullbrich, Y. Fan, M. Tropiano, K. A. McGarry, O. Zeika, M. K. Riede, C. J. Douglas, S. Barlow, S. R. Marder, D. Neher, D. Spoltore, K. Vandewal, *Nat. Energy* **2017**, 2, 17053.

[63] A. Al-Sharafi, *Self-Cleaning of Surfaces and Water Droplet Mobility*, **2019**.

[64] A. Mishra, N. Bhatt, A. K. Bajpai, in *Nanomaterials-Based Coatings*, DOI: https://doi.org/10.1016/B978-0-12-815884-5.00012-0 (Eds: P. Nguyen Tri, S. Rtimi, C. M. Ouellet Plamondon), Elsevier **2019**, p. 397.

[65] P. Li, Y. Zhang, Z. Chen, P. Gao, T. Wu, L.-M. Wang, *Sci. Rep.* **2017**, 7, 40547.

[66] S. Bertho, G. Janssen, T. J. Cleij, B. Conings, W. Moons, A. Gadisa, J. D'Haen, E. Goovaerts, L. Lutsen, J. Manca, D. Vanderzande, *Sol. Energy Mater. Sol. Cells* **2008**, 92, 753.

[67] C. Lindqvist, A. Sanz-Velasco, E. Wang, O. Bäcke, S. Gustafsson, E. Olsson, M. R. Andersson, C. Müller, *J. Mater. Chem. A* **2013**, 1, 7174.

[68] C.-Y. Liao, Y. Chen, C.-C. Lee, G. Wang, N.-W. Teng, C.-H. Lee, W.-L. Li, Y.-K. Chen, C.-H. Li, H.-L. Ho, P. H.-S. Tan, B. Wang, Y.-C. Huang, R. M. Young, M. R. Wasielewski, T. J. Marks, Y.-M. Chang, A. Facchetti, *Joule* **2020**, 4, 189.

[69] J. J. Michels, E. Moons, *Macromolecules* **2013**, 46, 8693.

[70] J. Xin, X. Meng, X. Xu, Q. Zhu, H. B. Naveed, W. Ma, *Matter* **2019**, 1, 1316.

[71] K. Shirzad, C. Viney, *J. R. Soc. Interface* **2023**, 20, 20230242.

[72] X. Y. Liu, *J. Chem. Phys.* **2000**, 112, 9949.

[73] A. Khaleghi, S. M. Sadrameli, M. Manteghian, *Rev. Inorg. Chem.* **2020**, 40, 167.

[74] A. Sauter, F. Roosen-Runge, F. Zhang, G. Lotze, A. Feoktystov, R. M. J. Jacobs, F. Schreiber, *Faraday Discuss.* **2015**, 179, 41.

[75] J. W. P. Schmelzer, *J. Non-Cryst. Solids* **2008**, 354, 269.

[76] L. Cormier, *Procedia Materials Science* **2014**, 7, 60.

[77] A. D. de Zerio, C. Müller, *Adv. Energy Mater.* **2018**, 8, 1702741.

[78] D. Kruk, E. Masiewicz, J. Budny, A. Stankiewicz, S. Lotarska, M. Oztop, Z. Wieczorek, *J. Food Eng.* **2022**, 317, 110848.

[79] C. A. Angell, *J. Phys. Chem. Solids* **1988**, 49, 863.

[80] J. Bergqvist, C. Lindqvist, O. Bäcke, Z. Ma, Z. Tang, W. Tress, S. Gustafsson, E. Wang, E. Olsson, M. R. Andersson, O. Inganäs, C. Müller, *J. Mater. Chem. A* **2014**, 2, 6146.

[81] M. Ghasemi, H. Hu, Z. Peng, J. J. Rech, I. Angunawela, J. H. Carpenter, S. J. Stuard, A. Wadsworth, I. McCulloch, W. You, H. Ade, *Joule* **2019**, 3, 1328.

[82] M. Ghasemi, N. Balar, Z. Peng, H. Hu, Y. Qin, T. Kim, J. J. Rech, M. Bidwell, W. Mask, I. McCulloch, W. You, A. Amassian, C. Risko, B. T. O'Connor, H. Ade, *Nat. Mater.* **2021**, 20, 525.

[83] L. Yu, D. Qian, S. Marina, F. A. A. Nugroho, A. Sharma, S. Hultmark, A. I. Hofmann, R. Kroon, J. Benduhn, D.-M. Smilgies, K. Vandewal, M. R. Andersson, C. Langhammer, J. Martín, F. Gao, C. Müller, *ACS Appl. Mater. Interfaces* **2019**, 11, 21766.

[84] S. Marina, A. D. Scaccabarozzi, E. Gutierrez-Fernandez, E. Solano, A. Khirbat, L. Ciammaruchi, A. Iturrospe, A. Balzer, L. Yu, E. Gabirondo, X. Monnier, H. Sardon, T. D. Anthopoulos, M. Caironi, M. Campoy-Quiles, C. Müller, D. Cangialosi, N. Stingelin, J. Martin, *Adv. Funct. Mater.* **2021**, 31, 2103784.

[85] A. Toda, in *Encyclopedia of Polymers and Composites*, DOI: 10.1007/978-3-642-37179-0_24-1 (Ed: S. Palsule), Springer Berlin Heidelberg, Berlin, Heidelberg **2021**, p. 1.

[86] J. Zhou, Y. Yang, Y. Yang, D. S. Kim, A. Yuan, X. Tian, C. Ophus, F. Sun, A. K. Schmid, M. Nathanson, H. Heinz, Q. An, H. Zeng, P. Ercius, J. Miao, *Nature* **2019**, 570, 500.

[87] R. Xie, A. R. Weisen, Y. Lee, M. A. Aplan, A. M. Fenton, A. E. Masucci, F. Kempe, M. Sommer, C. W. Pester, R. H. Colby, E. D. Gomez, *Nat. Commun.* **2020**, 11, 893.

[88] A. Sharma, X. Pan, J. A. Campbell, M. R. Andersson, D. A. Lewis, *Macromolecules* **2017**, 50, 3347.

[89] N. P. Holmes, M. Marks, P. Kumar, R. Kroon, M. G. Barr, N. Nicolaidis, K. Feron, A. Pivrikas, A. Fahy, A. D. d. Z. Mendaza, A. L. D. Kilcoyne, C. Müller, X. Zhou, M. R. Andersson, P. C. Dastoor, W. J. Belcher, *Nano Energy* **2016**, 19, 495.

[90] C. Lindqvist, J. Bergqvist, O. Bäcke, S. Gustafsson, E. Wang, E. Olsson, O. Inganäs, M. R. Andersson, C. Müller, *Appl. Phys. Lett.* **2014**, 104.

[91] Z. Ding, J. Kettle, M. Horie, S. W. Chang, G. C. Smith, A. I. Shames, E. A. Katz, *J. Mater. Chem. A* **2016**, 4, 7274.

[92] L. Ye, S. Li, X. Liu, S. Zhang, M. Ghasemi, Y. Xiong, J. Hou, H. Ade, *Joule* **2019**, 3, 443.

[93] C. Schäfer, S. Hultmark, Y. Yang, C. Müller, K. Börjesson, *Chem. Mater.* **2022**, 34, 9294.

[94] W. Yang, Z. Luo, R. Sun, J. Guo, T. Wang, Y. Wu, W. Wang, J. Guo, Q. Wu, M. Shi, H. Li, C. Yang, J. Min, *Nat. Commun.* **2020**, 11, 1218.

[95] P. Cheng, C. Yan, T.-K. Lau, J. Mai, X. Lu, X. Zhan, *Adv. Mater.* **2016**, 28, 5822.

[96] L. Derue, O. Dautel, A. Tournebize, M. Drees, H. Pan, S. Berthumeyrie, B. Pavageau, E. Cloutet, S. Chambon, L. Hirsch, A. Rivaton, P. Hudhomme, A. Facchetti, G. Wantz, *Adv. Mater.* **2014**, 26, 5831.

[97] Z. Li, H. C. Wong, Z. Huang, H. Zhong, C. H. Tan, W. C. Tsoi, J. S. Kim, J. R. Durrant, J. T. Cabral, *Nat. Commun.* **2013**, 4, 2227.

[98] F. Piersimoni, G. Degutis, S. Bertho, K. Vandewal, D. Spoltore, T. Vangerven, J. Drijkoningen, M. K. Van Bael, A. Hardy, J. D'Haen, W. Maes, D. Vanderzande, M. Nesladek, J. Manca, *J. Polym. Sci. B Polym. Phys.* **2013**, 51, 1209.

[99] H. Zhang, A. Borgschulte, F. A. Castro, R. Crockett, A. C. Gerecke, O. Deniz, J. Heier, S. Jenatsch, F. Nüesch, C. Sanchez-Sanchez, A. Zoladek-Lemanczyk, R. Hany, *Adv. Energy Mater.* **2015**, 5, 1400734.

[100] B. C. Schroeder, Z. Li, M. A. Brady, G. C. Faria, R. S. Ashraf, C. J. Takacs, J. S. Cowart, D. T. Duong, K. H. Chiu, C.-H. Tan, J. T. Cabral, A. Salleo, M. L. Chabinyc, J. R. Durrant, I. McCulloch, *Angew. Chem. Int. Ed.* **2014**, 53, 12870.

[101] W. Jiang, L. Ye, X. Li, C. Xiao, F. Tan, W. Zhao, J. Hou, Z. Wang, *Chem. Commun.* **2014**, 50, 1024.

[102] Y. Guo, Y. Li, O. Awartani, H. Han, J. Zhao, H. Ade, H. Yan, D. Zhao, *Adv. Mater.* **2017**, 29, 1700309.

[103] B. Watts, W. J. Belcher, L. Thomsen, H. Ade, P. C. Dastoor, *Macromolecules* **2009**, 42, 8392.

[104] L. Ye, H. Hu, M. Ghasemi, T. Wang, B. A. Collins, J.-H. Kim, K. Jiang, J. H. Carpenter, H. Li, Z. Li, T. McAfee, J. Zhao, X. Chen, J. L. Y. Lai, T. Ma, J.-L. Bredas, H. Yan, H. Ade, *Nat. Mater.* **2018**, 17, 253.

[105] N. D. Treat, M. A. Brady, G. Smith, M. F. Toney, E. J. Kramer, C. J. Hawker, M. L. Chabinyc, *Adv. Energy Mater.* **2011**, 1, 82.

[106] L. Ye, B. A. Collins, X. Jiao, J. Zhao, H. Yan, H. Ade, *Adv. Energy Mater.* **2018**, 8, 1703058.

[107] M. Hirami, *Macromol. Theory Simul.* **2010**, 19, 432.

[108] P. R. Couchman, *Phys. Lett. A* **1979**, 70, 155.

[109] I. R. Henriques, L. A. Borges, M. F. Costa, B. G. Soares, D. A. Castello, *Polym Test.* **2018**, 72, 394.

[110] S. Ebnesajjad, in *Surface Treatment of Materials for Adhesive Bonding (Second Edition)*, DOI: https://doi.org/10.1016/B978-0-323-26435-8.00004-6 (Ed: S. Ebnesajjad), William Andrew Publishing, Oxford **2014**, p. 39.

[111] P. Gill, T. T. Moghadam, B. Ranjbar, *Journal of biomolecular techniques : JBT* **2010**, 21 4, 167.

[112] M. E. Brown, in *Introduction to Thermal Analysis: Techniques and applications*, DOI: 10.1007/978-94-009-1219-9_4 (Ed: M. E. Brown), Springer Netherlands, Dordrecht **1988**, p. 23.

[113] M. TOLEDO, The Revolutionary Flash DSC 1, https://www.mt.com/sg/en/home/supportive_content/matchar_apps/MatChar_UC323.html, accessed: 2023-09-29.

[114] C. Schick, R. Androsch, in *Thermal Analysis of Polymeric Materials*, DOI: https://doi.org/10.1002/9783527828692.ch3 **2022**, p. 75.

[115] C. Müller, J. Bergqvist, K. Vandewal, K. Tvingstedt, A. S. Anselmo, R. Magnusson, M. I. Alonso, E. Moons, H. Arwin, M. Campoy-Quiles, O. Inganäs, *J. Mater. Chem.* **2011**, 21, 10676.

[116] J. Zhao, A. Swinnen, G. Van Assche, J. Manca, D. Vanderzande, B. V. Mele, *J. Phys. Chem. B* **2009**, 113, 1587.

[117] C. Bruner, F. Novoa, S. Dupont, R. Dauskardt, *ACS Appl. Mater. Interfaces* **2014**, 6, 21474.

[118] D. Leman, M. A. Kelly, S. Ness, S. Engmann, A. Herzing, C. Snyder, H. W. Ro, R. J. Kline, D. M. DeLongchamp, L. J. Richter, *Macromolecules* **2015**, 48, 383.

[119] E. Gutierrez-Fernandez, A. D. Scaccabarozzi, A. Basu, E. Solano, T. D. Anthopoulos, J. Martín, *Adv. Sci.* **2022**, 9, 2104977.

[120] C. A. Angell, *J. Non-Cryst. Solids* **1991**, 131-133, 13.

[121] H. Gong, M. Sun, Z. Li, R. Liu, Y. Tian, L.-M. Wang, *Eur. Phys. J. E.* **2011**, 34, 86.

[122] R. Tao, E. Gurung, M. M. Cetin, M. F. Mayer, E. L. Quitevis, S. L. Simon, *Thermochim. Actra* **2017**, 654, 121.

[123] K. F. Kelton, *J. Condens. Matter Phys.* **2017**, 29, 023002.

[124] V. N. Novikov, A. P. Sokolov, in *Entropy*, Vol. 24, 2022.

[125] G. Tammann, W. Hesse, *Z. Anorg. Allg. Chem.* **1926**, 156, 245.

[126] J. J. de Pablo, *Nat. Mater.* **2020**, 19, 1041.

[127] S. L. Webb, *Contrib. Mineral. Petrol.* **2021**, 176, 78.

[128] S. Gao, S. L. Simon, *Thermochim. Actra* **2015**, 603, 123.

[129] N. Shamim, Y. P. Koh, S. L. Simon, G. B. McKenna, *J. Polym. Sci. B Polym. Phys.* **2014**, 52, 1462.

[130] C. T. MOYNIHAN, A. J. EASTEAL, M. A. De BOLT, J. TUCKER, *J. Am. Ceram. Soc.* **1976**, 59, 12.

[131] S. Gao, Y. P. Koh, S. L. Simon, *Macromolecules* **2013**, 46, 562.

[132] S. Hultmark, A. Cravcenco, K. Kushwaha, S. Mallick, P. Erhart, K. Börjesson, C. Müller, *Sci. Adv.* **2021**, 7, eabi4659.

[133] C. Müller, *Chem. Mater.* **2015**, 27, 2740.

[134] N. D. Treat, T. E. Mates, C. J. Hawker, E. J. Kramer, M. L. Chabinyc, *Macromolecules* **2013**, 46, 1002.

[135] D. Huang, G. B. McKenna, *J. Chem. Phys.* **2001**, 114, 5621.

[136] D. Turnbull, *Contemp. Phys.* **1969**, 10, 473.

[137] K. Amann-Winkel, C. Gainaru, P. H. Handle, M. Seidl, H. Nelson, R. Böhmer, T. Loerting, *Proc. Nati. Acad. Sci.* **2013**, 110, 17720.

[138] V. N. Novikov, Y. Ding, A. P. Sokolov, *Phys. Rev. E* **2005**, 71, 061501.

[139] L. Yu, X. Li, E. Pavlica, F. P. V. Koch, G. Portale, I. da Silva, M. A. Loth, J. E. Anthony, P. Smith, G. Bratina, B. K. C. Kjellander, C. W. M. Bastiaansen, D. J. Broer, G. H. Gelinck, N. Stingelin, *Chem. Mater.* **2013**, 25, 1823.

[140] L. Yu, G. Portale, N. Stingelin, *J. Mater. Chem. C* **2021**, 9, 10547.

[141] S. Hultmark, M. Craighero, S. Zokaei, D. Kim, E. Järsvall, F. Farooqi, S. Marina, R. Kroon, J. Martin, I. Zozoulenko, C. Müller, *J. Mater. Chem. C* **2023**, 11, 8091.

[142] S. H. K. Paleti, S. Hultmark, J. Han, Y. Wen, H. Xu, S. Chen, E. Järsvall, I. Jalan, D. R. Villalva, A. Sharma, J. I. Khan, E. Moons, R. Li, L. Yu, J. Gorenflot, F. Laquai, C. Müller, D. Baran, *Nat. Commun.* **2023**, 14, 4608.

[143] M. Glatthaar, M. Riede, N. Keegan, K. Sylvester-Hvid, B. Zimmermann, M. Niggemann, A. Hinsch, A. Gombert, *Sol. Energy Mater. Sol. Cells* **2007**, 91, 390.

[144] K. Feron, T. J. Nagle, L. J. Rozanski, B. B. Gong, C. J. Fell, *Sol. Energy Mater. Sol. Cells* **2013**, 109, 169.

[145] T. S. Glen, N. W. Scarratt, H. Yi, A. Iraqi, T. Wang, J. Kingsley, A. R. Buckley, D. G. Lidzey, A. M. Donald, *Sol. Energy Mater. Sol. Cells* **2015**, 140, 25.

[146] A. Sharma, G. Andersson, D. A. Lewis, *Phys. Chem. Chem. Phys.* **2011**, 13, 4381.

[147] F. Wang, Z. a. Tan, Y. Li, *Energy Environ. Sci.* **2015**, 8, 1059.

[148] C.-C. Chueh, C.-Z. Li, A. K. Y. Jen, *Energy Environ. Sci.* **2015**, 8, 1160.

[149] P. Cheng, X. Zhan, *Chem. Soc. Rev.* **2016**, 45, 2544.

[150] C. Xie, X. Tang, M. Berlinghof, S. Langner, S. Chen, A. Späth, N. Li, R. H. Fink, T. Unruh, C. J. Brabec, *ACS Appl. Mater. Interfaces* **2018**, 10, 23225.

[151] I. T. Sachs-Quintana, T. Heumüller, W. R. Mateker, D. E. Orozco, R. Cheacharoen, S. Sweetnam, C. J. Brabec, M. D. McGehee, *Adv. Funct. Mater.* **2014**, 24, 3978.

[152] K. Zhang, R. Xia, B. Fan, X. Liu, Z. Wang, S. Dong, H.-L. Yip, L. Ying, F. Huang, Y. Cao, *Adv. Mater.* **2018**, 30, 1803166.

[153] J. D. Mcbrayer, R. M. Swanson, T. W. Sigmon, **1983**.

[154] E. Wimmer, W. Wolf, J. Sticht, P. Saxe, C. B. Geller, R. Najafabadi, G. A. Young, *Phys. Rev. B* **2008**, 77, 134305.

[155] L. Duan, A. Uddin, *Adv. Sci.* **2020**, 7, 1903259.

[156] S. T. Lee, Z. Q. Gao, L. S. Hung, *Appl. Phys. Lett.* **1999**, 75, 1404.

[157] R. Rösch, D. M. Tanenbaum, M. Jørgensen, M. Seeland, M. Bärenklau, M. Hermenau, E. Voroshazi, M. T. Lloyd, Y. Galagan, B. Zimmermann, U. Würfel, M. Hösel, H. F. Dam, S. A. Gevorgyan, S. Kudret, W. Maes, L. Lutsen, D. Vanderzande, R. Andriessen, G. Teran-Escobar, M. Lira-Cantu, A. Rivaton, G. Y. Uzunoğlu, D. Germack, B. Andreasen, M. V. Madsen, K. Norrman, H. Hoppe, F. C. Krebs, *Energy Environ. Sci.* **2012**, 5, 6521.

[158] E. Voroshazi, G. Uytterhoeven, K. Cnops, T. Conard, P. Favia, H. Bender, R. Muller, D. Cheyns, *ACS Appl. Mater. Interfaces* **2015**, 7, 618.

[159] R. Franke, B. Maennig, A. Petrich, M. Pfeiffer, *Sol. Energy Mater. Sol. Cells* **2008**, 92, 732.

[160] A. Uddin, M. B. Upama, H. Yi, L. Duan, *Coat.* **2019**, 9, 65.

[161] M. Salvador, N. Gasparini, J. D. Perea, S. H. Paleti, A. Distler, L. N. Inasaridze, P. A. Troshin, L. Lüer, H.-J. Egelhaaf, C. Brabec, *Energy Environ. Sci.* **2017**, 10, 2005.

[162] A. Dazzi, C. B. Prater, *Chem. Rev.* **2017**, 117, 5146.